

1 **Measurement report: Validation of multi-satellite remote sensing**
2 **products and potential source apportionment of BrO and IO in the**
3 **Arctic using ship-based DOAS**

4 Qijin Zhang^{1,2}, Chengzhi Xing^{2,*}, Yikai Li^{2,5}, Haochen Peng^{1,2}, Haoran Liu⁶, Chao Liu^{1,2}, Zhiguo
5 Zhang^{1,2}, Wanchao Ma¹, Tianyu Tang¹, Cheng Liu^{1,2,3,4,*}

6 ¹Department of Precision Machinery and Precision Instrumentation, University of Science and
7 Technology of China, Hefei 230026, China

8 ²Key Lab of Environmental Optics & Technology, Anhui Institute of Optics and Fine Mechanics,
9 Hefei Institutes of Physical Science, Chinese Academy of Sciences, Hefei 230031, China

10 ³Center for Excellence in Regional Atmospheric Environment, Institute of Urban Environment,
11 Chinese Academy of Sciences, Xiamen 361021, China

12 ⁴Key Laboratory of Precision Scientific Instrumentation of Anhui Higher Education Institutes,
13 University of Science and Technology of China, Hefei 230026, China

14 ⁵School of Environmental Science and Optoelectronic Technology, University of Science and
15 Technology of China, Hefei 230026, China

16 ⁶Information Materials and Intelligent Sensing Laboratory of Anhui Province, Institutes of
17 Physical Science and Information Technology, Anhui University, Hefei, 230601, China

18 Corresponding authors: xingcz@aiofm.ac.cn; chliu81@ustc.edu.cn
19

20 **Abstract:**

21 Arctic reactive halogen species (RHS) are pivotal in mediating polar air-sea interactions and
22 global biogeochemical cycling. Based on ship-borne MAX-DOAS observations from the 12th
23 Chinese National Arctic Research Expedition (July to September 2021), this study provides a
24 systematic performance assessment of TROPOMI, GEMS, and GOME-2 satellite products in the
25 Arctic ($R > 0.6$). Our findings indicate that tropospheric BrO variability is predominantly
26 governed by sea-ice contact (SIC) duration, accounting for 48.63% of the variance in a
27 Generalized Additive Model (GAM). Potential BrO source regions are identified in western
28 Greenland, the high-latitude Canadian Arctic, and the Marginal Ice Zone (MIZ). Implementing a
29 dynamic boundary layer height (BLH) constraint enhanced the correlation from 0.73 to 0.77.
30 Meteorological conditions exert significant modulation on activation efficiency. For instance,
31 correlations reached 0.84 under southwesterly flow, whereas snowfall reduced the correlation
32 from 0.84 during snow-free periods to 0.61 during snowfall events. Conversely, IO spatial
33 variability is primarily driven by marine biogenic emissions, exhibiting a positive correlation with
34 chlorophyll-a concentrations ($R = 0.64$) and clustering in phytoplankton-rich regions such as the

Bering Strait. In the MIZ, the moderate correlation between BrO and IO ($R = 0.5$) suggests their co-evolution at the shared ice-ocean-atmosphere interface. These high-resolution datasets provide critical a priori constraints for atmospheric chemistry models. Specifically, they facilitate the optimization of polar emission parameterizations and reactive halogen budgets, thereby enhancing the predictive accuracy of GEOS-Chem and WRF-Chem for polar atmospheric processes and improving the robustness of global climate assessments.

1. Introduction

The unique geographic and climatic conditions of the polar regions make them sensitive indicators and amplifiers for global climate change and atmospheric chemistry. They play an irreplaceable role in regulating global ozone balance, aerosol cycles, and air-sea interactions (Polvani et al., 2020). Nitrogen oxides (NO_x), formaldehyde (HCHO), and RHS, including X, HOX, XY, OXO, XNO_2 , X_2 , XO, and XONO_2 , where Y and X represent halogen atoms such as I and Br are core components of polar atmospheric chemistry (Hara et al., 2020; Saiz-Lopez et al., 2008). Halogen radicals (e.g., Br, I, Cl) drive polar ozone depletion catalytically (Hara et al., 2020; Polvani et al., 2020), while RHS also modulate the HO_x and NO_x ratios (Bloss et al., 2005; Khosravi et al., 2020; Ranjithkumar et al., 2023). XO radicals oxidize NO to NO_2 , thus increasing the NO_x ratio; in contrast, they react with HO_2 to form HOX, which subsequently undergoes photolysis (a process particularly efficient for HOI) to generate OH, thereby decreasing the HO_x ratio (Saiz-Lopez et al., 2007; Welsh et al., 2023). The bromine explosion process on saline surfaces covered by sea ice or snow converts bromide ions (Br^-) into gaseous reactive bromine species, serving as the primary source of bromine in the polar boundary layer (Hara et al., 2020; Saiz-Lopez et al., 2007). In contrast, iodine oxides (IO) originate mainly from marine phytoplankton, with their concentrations tightly linked to polar ecosystem dynamics (Cuevas et al., 2018). Fig. S1 illustrates the key chemical cycles of iodine and bromine in the polar troposphere.

Currently, polar atmospheric composition observations primarily rely on satellite remote sensing (Begoïn et al., 2010; Blechschmidt et al., 2016; Bougoudis et al., 2020; Dameris et al., 2021; De Laat et al., 2024; Hindley et al., 2019; Mahajan et al., 2021; Roy et al., 2024; Seo et al., 2020; Yang et al., 2021) and ground-based station measurements (Crutzen, 1970; Frieß et al., 2010, 2011; Gong et al., 2025; Hao et al., 2025; Luo et al., 2018; Mahajan et al., 2021, 2024; Prados-Roman et al., 2018), yet both suffer from notable limitations. While satellite remote sensing enables large scale coverage, the unique high albedo snow and ice surfaces, extreme low temperatures, and high cloud cover in polar regions limit its retrieval accuracy for trace gases, particularly low concentration BrO and IO. Furthermore, the spatiotemporal resolution of satellites is insufficient to capture the rapid dynamics of polar photochemical reactions (e.g., reactive bromine radicals have lifetimes as short as minutes), precluding real-time tracking of short-term trace gas variations (Wagner et al., 2007). Ground-based stations deliver high resolution data but are predominantly located in terrestrial or island regions of Antarctica and the Arctic (Frieß et al.,

72 2011; Luo et al., 2018; Prados-Roman et al., 2018; Simpson et al., 2017; Yang et al., 2020). Since
73 approximately 70% of polar areas consist of oceans, data on NO₂, HCHO, and BrO in the marine
74 boundary layer are scarce. This scarcity means satellite retrieval results over oceanic regions lack
75 effective validation.

76 Additionally, regional studies of reactive halogen species exhibit distinct gaps: most research
77 on BrO and IO focuses on local regions like the Antarctic Peninsula and Arctic Svalbard (Adachi
78 et al., 2022; Čížková et al., 2023; Luo et al., 2018; Mahajan et al., 2024; Park et al., 2023;
79 Spagnesi et al., 2024), with ship-based DOAS data missing for extensive oceanic areas such as the
80 Arctic Chukchi and Beaufort Seas. Extensive literature over the past few decades has established
81 the foundation for research on polar halogen activation (Brockway et al., 2024; Luo et al., 2018;
82 Peterson et al., 2017; Pratt et al., 2013; Swanson et al., 2020; Wagner et al., 2007), particularly
83 regarding the distribution and underlying mechanisms of reactive halogens during the polar spring.
84 Specifically, Pratt et al. (2013) confirmed the photochemical production of Br₂ from sunlit
85 snowpack, while Swanson et al. (2020) identified distinct environmental patterns of reactive
86 bromine events through long-term ground-based observations. However, existing datasets
87 primarily analyze springtime data and are concentrated at stationary sites such as Alert, Utqiagvik,
88 and Ny-Ålesund. Observational evidence for the summer melt season remains scarce, leaving the
89 evolution mechanisms of the halogen cycle under continuous high-radiation conditions unclear.
90 Thus, there is an urgent need for mobile, high spatiotemporal resolution on-site detection
91 techniques to resolve polar boundary layer chemical processes and accurately identify the sources
92 and transformations of halogen species. Ship-based Multi-Axis Differential Optical Absorption
93 Spectroscopy (MAX-DOAS) is well suited to address this gap: by collecting scattered sunlight
94 from multiple directions, it retrieves IO, BrO, HCHO, and other trace gases from the ultraviolet
95 visible spectrum. Moreover, it enables point-line integrated mobile observations aboard research
96 vessels, serving as a robust tool for studying atmospheric composition in polar oceanic regions
97 (Nasse et al., 2015a, b; Wagner et al., 2007).

98 In recent years, Arctic sea-ice extent has exhibited a significant declining trend, which
99 directly impacts key processes in polar atmospheric chemistry (e.g., the extent and intensity of
100 bromine explosions). Significant reductions in Arctic sea-ice extent and concentration were
101 observed in August 2021, particularly in the Beaufort Sea and Bering Strait (Fig. S2). These
102 changes alter the saline water-sea surface-atmosphere exchange interface and influence marine
103 phytoplankton distribution, which may further modulate the release and formation of reactive
104 halogen species.

105 Leveraging the ship-based MAX-DOAS measurements aboard the Xuelong 2 during China's
106 12th Arctic Scientific Expedition (2021), this study pursued the following objectives consistent
107 with the nature of a Measurement Report: 1) Evaluate the polar applicability of NO₂, HCHO, and
108 BrO satellite products by providing a high-precision on-site benchmark for validating retrieval

109 uncertainties in polar oceanic regions. 2) The sea-ice-driven mechanism governing tropospheric
110 BrO was validated, with the quantification of sea-ice contact (SIC) duration refined by
111 incorporating boundary layer height constraints. Furthermore, Generalized Additive Models
112 (GAMs) were employed to elucidate the synergistic influences of meteorological parameters and
113 sea-ice surface characteristics on the BrO - SIC relationship. 3) Verify the biogenic driving
114 mechanism of IO concentrations by quantifying its correlation with MODIS-derived chlorophyll-a
115 and revealing the spatial differentiation between sea-ice-derived BrO and biogenic IO. By filling
116 critical observational gaps in the Arctic marine boundary layer, this report provides essential
117 empirical constraints for upgrading the parameterizations of halogen chemical cycles in
118 atmospheric chemistry models (e.g., GEOS-Chem and WRF-Chem), thereby enhancing the
119 accuracy of polar air-sea interaction simulations and global climate assessments.

120 **2. Experiment**

121 **2.1 Experimental Setup**

122 The instrument was installed on the research vessel Xuelong 2 on July 10, 2021, and
123 performed continuous automated measurements throughout the cruise. The vessel departed
124 Shanghai Port (31.35°N, 121.69°E) on July 12, 2021, sailing via the Korea Strait, Soya Strait,
125 Bering Strait, Beaufort Sea, and Siberian Seas (see Fig. 1 for the detailed trajectory). The time of
126 the first contact with sea ice was July 24 (72.20°N, 169.18°W); subsequently, the vessel sailed
127 toward the Arctic region and began its return voyage on August 28, 2021. The instrument was
128 fixed on the vessel's side deck, mounted away from the ship's exhaust vents with an unobstructed
129 surrounding field of view (Tan et al., 2018). During ship-based mobile measurements, the
130 observation azimuth was directed toward the stern (see Fig. S3 for the vessel's top view). The
131 ship-based MAX-DOAS system comprises a motor driven observation unit, a spectrometer
132 operating in the 300-460 nm range (spectral resolution: 0.6 nm), a temperature control system, and
133 a computer control unit. For measurements, right angle prisms reflect scattered sunlight at
134 different elevation angles; this light is transmitted to the spectrometer via optical fibers for spectral
135 acquisition, and the computer control unit performs spectral analysis. The temperature control
136 system ensured stable instrument operation under the Arctic's extreme cold conditions. Ship sway
137 caused the telescope's elevation angle relative to the vessel to deviate from the actual observation
138 direction. To mitigate this effect, the spectral exposure time was set to 100 ms, which is short
139 enough that ship movement during spectral recording was negligible. Additionally, the observation
140 elevation angle sequence was set to 10°, 20°, and 90° (zenith) to reduce the impact of ship roll on
141 the observed spectra. The system was also equipped with a high precision Global Positioning
142 System to log the vessel's real time cruise coordinates and trajectory.

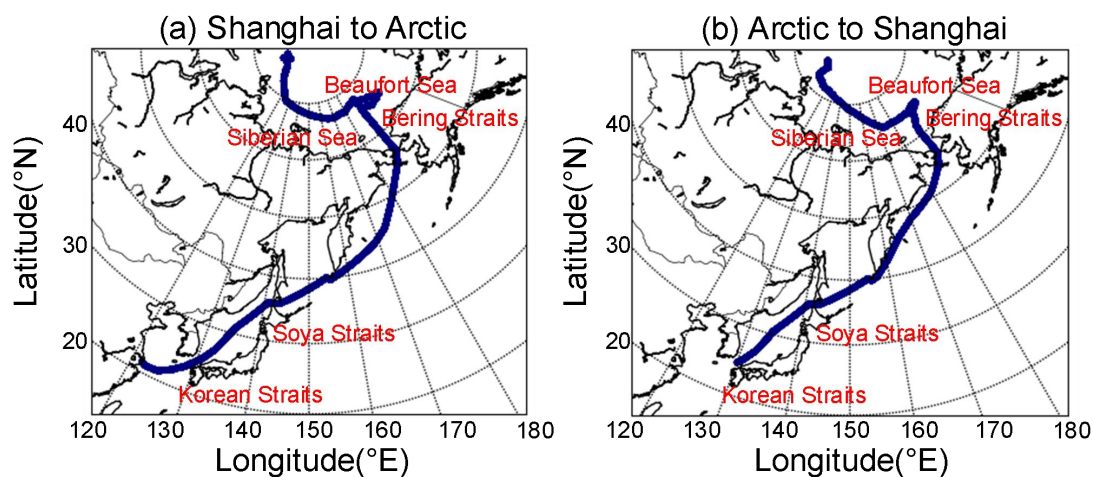


Fig. 1. Trajectories of the research vessel for the 12th Arctic Scientific Expedition: (a) Go from Shanghai to the Arctic; (b) Return from the Arctic

2.2 Data Analysis

2.2.1 Data Processing and Filtering

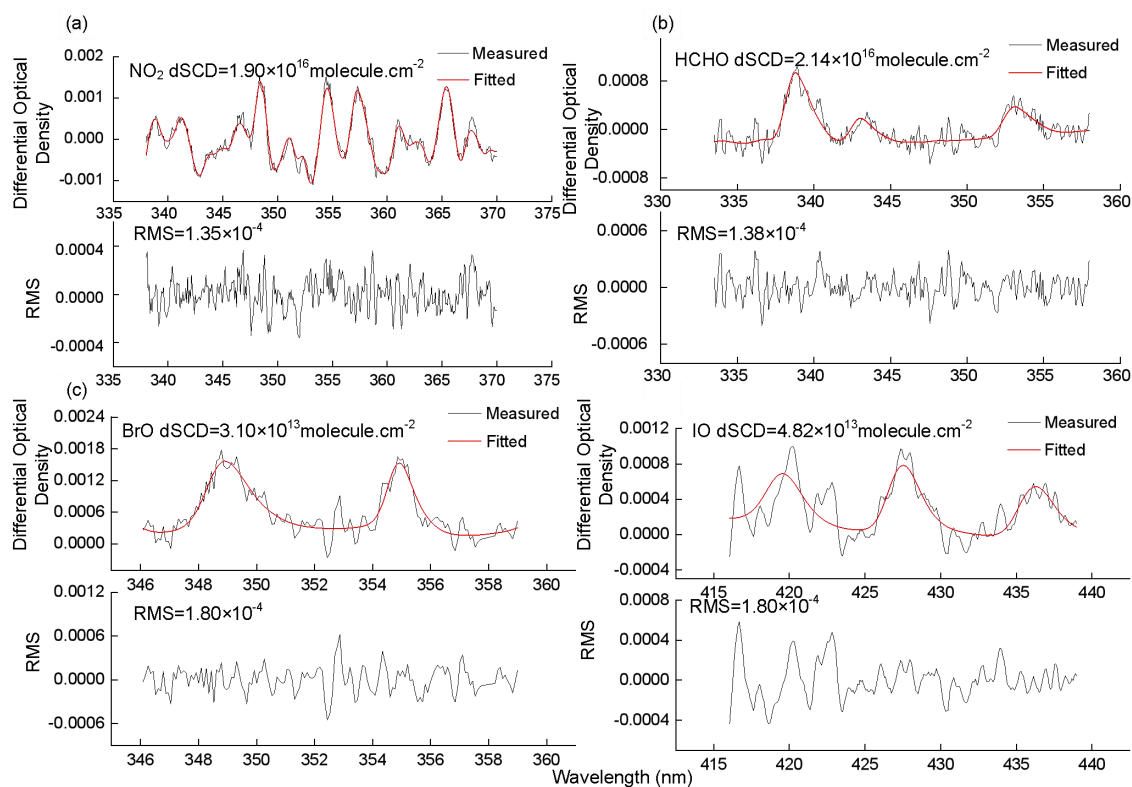
Data retrieval was conducted using the QDOAS software (BIRA-IASB; <http://uv-vis.aeronomie.be/software/QDOAS>) based on the DOAS principle. For ship-based spectral processing, offset corrections and dark current were first applied to the data. During retrieval, zenith spectra for each elevation angle sequence were used as reference spectra. Detailed retrieval parameters are provided in Table 1, with retrieval configurations following previous studies (Frieß et al., 2023; Hong et al., 2018; Mahajan et al., 2021; Saiz-Lopez et al., 2008). A 5th-order polynomial was used to remove broad band structures induced by Mie and Rayleigh scattering, while a nonlinear intensity offset was incorporated into the fitting process to mitigate the impact of instrument stray light.

Table 1. Retrieval settings of IO, BrO, HCHO, and NO₂

| Parameter | Reference | Fitting intervals (nm) | | | |
|------------------------|------------------------------|------------------------|-----------|---------|---------|
| | | NO ₂ | HCHO | BrO | IO |
| | Fitting wavelength | 338-370 | 336.5-359 | 346-358 | 416-439 |
| NO ₂ (298K) | (Vandaele et al., 1998) | √ | √ | √ | √ |
| NO ₂ (220K) | (Vandaele et al., 1998) | √ | √ | √ | √ |
| HCHO (298K) | (Meller and Moortgat, 2000) | √ | √ | × | √ |
| HONO (296K) | (Stutz et al., 2000) | × | × | √ | √ |
| O ₃ (243K) | (Serdyuchenko et al., 2014) | √ | × | √ | √ |
| O ₃ (223K) | (Serdyuchenko et al., 2014) | √ | × | √ | √ |
| O ₄ (293K) | (Thalman and Volkamer, 2013) | √ | √ | √ | √ |
| BrO (223K) | (Fleischmann et al., 2004) | √ | √ | √ | × |
| H ₂ O | (Rothman et al.2009) | × | × | × | √ |

| | | | | | |
|-------------------|------------------------------------|-----------|-----------|-----------|-----------|
| IO | (Carlos Gómez Martín et al., 2005) | × | × | × | √ |
| Ring | Calculated with QDOAS | √ | √ | √ | √ |
| Polynomial degree | | 5th order | 5th order | 5th order | 3rd order |
| Intensity offset | | Constant | Constant | Constant | Constant |

158 Ship-based MAX-DOAS retrieves differential slant column densities (DSCDs) using
 159 sequential zenith reference spectra, which effectively eliminates the stratospheric background and
 160 enables the detection of tropospheric trace gases. To compensate for minor changes in
 161 spectrometer spectral calibration, spectral shift and stretching were incorporated during the fitting
 162 process. Fig. 2 presents a typical spectral fitting result for a spectrum measured at 10° elevation at
 163 1:02 UTC on August 15, 2021. Only retrieval values with a root mean square (RMS) < 3×10^{-3} and
 164 SZA < 75° were retained in this study. During mobile measurements, the ship's exhaust plume
 165 could interfere with trace gas measurements under unfavorable wind conditions. To eliminate ship
 166 exhaust interference with the spectra, spectral data measured at ship speeds below 5 km/h were
 167 filtered out, and spectra acquired under unfavorable wind conditions (0°-90° and 315°-360°) were
 168 excluded. A schematic representation of these filtering criteria is provided in Fig. S3. The filtered
 169 dataset remained adequate for robust analysis (Behrens et al., 2019).



170
 171 **Fig. 2.** An example of Ship MAX-DOAS spectral fittings for (a) NO₂, (b) HCHO, (c) BrO, and (d)
 172 IO. The spectrum was recorded at 1: 02 UTC on August 15, 2021, with an elevation of 10°.

2.2.2 Uncertainties in Stratospheric-Tropospheric Separation

The separation of tropospheric and stratospheric contributions using DSCDs involves several layers of uncertainty. Following established error assessment methodologies (Hendrick et al., 2007; Tack et al., 2015; Wittrock et al., 2004), the total uncertainty in our retrieved tropospheric vertical columns is attributed to two primary factors. First, spectral noise and statistical fitting uncertainties account for approximately 5% to 10% of the DSCD error under clear-sky conditions. Second, uncertainties arise from atmospheric spatial inhomogeneity and stratospheric photochemical gradients. These gradients are particularly pronounced for reactive species such as NO₂ and BrO. To mitigate this, we restricted our analysis to observations with SZA < 75°, ensuring that the stratosphere remained in a photochemical quasi-steady state. Additionally, the implementation of a sequential zenith reference spectrum (ZRS) within short intervals (a few minutes) effectively minimizes the influence of stratospheric temporal and spatial variability. In the Arctic environment, the residual error stemming from stratospheric gradients following the sequential ZRS subtraction is estimated to be less than 10%.

Based on these components, the combined uncertainty for the tropospheric and stratospheric separation during this campaign ranges from 11.2% to 14.1%. We note that the relative uncertainty may increase in the pristine Arctic atmosphere when tropospheric abundances are near detection limits.

2.2.3 Retrieval of Trace Gas Vertical Column Densities

Because DOAS analysis yielded DSCDs in this study, conversion to vertical column densities (VCDs) required the application of differential atmospheric air mass factors, and the specific formula is given below:

$$\begin{aligned} DSCD_{trop}(\alpha) &= SCD_{trop}(\alpha) - SCD_{trop}(90^\circ) \\ &= AMF_{trop}(\alpha) \times VCD_{trop} - AMF_{trop}(90^\circ) \times VCD_{trop} \\ \Rightarrow VCD_{trop} &= \frac{DSCD_{trop}(\alpha)}{DAMF_{trop}(\alpha)} \end{aligned} \quad (1)$$

In the above equation, α denotes the telescope observation angle, and $DAMF_{trop}(\alpha)$ is expressed as $AMF_{trop}(\alpha) - AMF_{trop}(90^\circ)$. Owing to rapidly changing radiative conditions and heterogeneous air masses encountered during ship-based MAX-DOAS campaigns, an alternative retrieval method was developed for mobile platforms. This method, which has been successfully applied in previous mobile MAX-DOAS studies (Hong et al., 2018; Wagner et al., 2010), demonstrates superior performance over the standard approach. Therefore, this study adopts this method to retrieve tropospheric VCDs, with the specific formula provided below:

$$\begin{aligned} VCD_{trop} &= \frac{SCD_{meas}(\alpha) - SCD_{strat}(SZA)}{AMF_{trop}(\alpha)} \\ &= \frac{DSCD_{meas}(\alpha) + SCD_{ref} - SCD_{strat}(SZA)}{AMF_{trop}(\alpha)} \end{aligned} \quad (2)$$

In the above equation, SZA denotes the Solar Zenith Angle. The difference between

205 SCD_{ref} and SCD_{strat} (SZA) two unknowns) is defined as $DSCD_{offset}$. Combining Equations (1)
 206 and (2) yields the specific expression for $DSCD_{offset}$.

$$207 \quad DSCD_{offset} = \frac{DSCD_{meas}(\alpha) \times AMF_{trop}(90^\circ) - DSCD_{meas}(90^\circ) \times AMF_{trop}(\alpha)}{AMF_{trop}(\alpha) - AMF_{trop}(90^\circ)} \quad (3)$$

208 Here, $DSCD_{offset}$ is a time smooth function, fitted to the $DSCD_{offset}(t_i)$ time series using a second
 209 order polynomial, where t_i denotes the time interval between two spectra at a given observation
 210 angle. The calculated $DSCD_{offset}(t_i)$ time series is expressed as:

$$211 \quad \begin{aligned} & DSCD_{offset}(t_i) \\ & = \frac{DSCD_{meas}(\alpha, t_i) \times AMF_{trop}(90^\circ, t_i) - DSCD_{meas}(90^\circ, t_i) \times AMF_{trop}(\alpha, t_i)}{AMF_{trop}(\alpha, t_i) - AMF_{trop}(90^\circ, t_i)} \end{aligned} \quad (4)$$

212 The fitted polynomial approximates $DSCD_{offset}(t_i)$; substituting it into Equation (2) gives the
 213 tropospheric VCD time series. Details of this method are provided in Wagner et al. (2010).
 214 Radiative calculations in this study were conducted with the atmospheric radiative transfer model
 215 SCIATRAN 2.2 (Rozanov et al., 2005).

216 **2.3 Performance of the MAX-DOAS Retrieval**

217 **2.3.1 Uncertainty Analysis**

218 **Following established methodologies** (Hendrick et al., 2007; Song et al., 2023; Tack et al.,
 219 2015; Wagner et al., 2007; Wittrock et al., 2004), **the uncertainty in MAX-DOAS retrievals is**
 220 **categorized into four primary sources. First, smoothing and noise errors originate from statistical**
 221 **uncertainties in the DOAS fitting. Under clear-sky conditions, the fitting errors for NO₂, HCHO,**
 222 **BrO, and IO remain within 5% to 10%. Second, reference spectrum uncertainty arises because**
 223 **tropospheric DSCDs are determined by subtracting a sequential ZRS from off-axis measurements.**
 224 **While this approach assumes stratospheric absorption cancels out, uncertainties in the residual**
 225 **trace gas abundances within the ZRS (stemming from stratospheric background or tropospheric**
 226 **pollution) can introduce systematic biases of approximately 10% to 15%. Third, algorithmic errors**
 227 **primarily stem from uncertainties in aerosol vertical distribution, multiple scattering simulations,**
 228 **and profile assumptions within the radiative transfer model. For the Arctic sea-ice environment,**
 229 **sensitivity tests demonstrate that surface albedo has a negligible impact on boundary layer**
 230 **observations at low elevation angles, with the total AMF uncertainty estimated at 10% to 20%.**
 231 **Fourth, residual errors from stratospheric gradients and atmospheric inhomogeneity are considered.**
 232 **By employing the sequential ZRS method and filtering for SZA < 75°, errors from steep**
 233 **stratospheric photochemical gradients are effectively suppressed to within 10%.**

234 **Consequently, the total uncertainty of the retrieved VCDs during this ship-based campaign is**
 235 **estimated to be approximately 18.1% to 28.7%. Furthermore, due to the pristine background of the**
 236 **Arctic region, the relative proportion of this uncertainty may increase when tropospheric**
 237 **concentrations are extremely low. Detailed information is provided in the supplement (Table S1).**

2.3.2 Detection Limits

To evaluate the sensitivity of MAX-DOAS in the Arctic environment, different methods were adopted to calculate detection limits based on the atmospheric distribution and signal-to-noise ratio characteristics of various trace gases. First, for NO₂, HCHO, and IO, we used the standard method in DOAS applications to determine the detection limit (Chance and Spurr, 1997; Stutz and Platt, 1996; Wagner et al., 2007). The detection limit of the DSCD (LOD_{dscd}) is defined as twice the statistical fitting error from the DOAS retrieval ($2\sigma_{fit}$). Second, for BrO, since tropospheric BrO concentrations in the Arctic are relatively low and influenced by the stratospheric BrO background, the conventional $2\sigma_{fit}$ noise method often over estimates the tropospheric detection limit because of the high weighting of stratospheric absorption. Therefore, we adopted the equivalent RMS noise factor method, which calculates the minimum identifiable slant column density at a given signal-to-noise ratio by analyzing the RMS noise of the residual spectrum (Coburn et al., 2011). During the observation period, the estimated detection limits for NO₂, HCHO, BrO, and IO were 2.0×10^{15} molec.cm⁻², 5.0×10^{15} molec.cm⁻², 3.0×10^{13} molec.cm⁻², 1.3×10^{13} molec.cm⁻², respectively.

2.4 Satellite Observations

This study compares ship-based MAX-DOAS measurements with tropospheric VCD products from multiple satellite instruments, including the Tropospheric Monitoring Instrument (TROPOMI), Geostationary Environmental Monitoring Spectrometer (GEMS), and Global Ozone Monitoring Experiment-2 (GOME-2).

TROPOMI is onboard the Sentinel-5P (S-5P) satellite, operating in a near Earth sun synchronous orbit with an equator crossing time of 13:30 local time. It features 4 independent spectrometers covering the mid-ultraviolet (UV), long wave UV-visible (UV-VIS), short-wave infrared (SWIR), and near infrared (NIR) bands, with a total wavelength range of 270-2385 nm (non-overlapping and discontinuous). Among comparable atmospheric remote sensing instruments, TROPOMI has the best spatial resolution (5.5 km × 3.5 km), enabling precise capture of spatial distributions of trace gases in small scale regions, making it a key data source for high resolution atmospheric composition monitoring in polar oceans.

GEMS is a hyperspectral UV-VIS imaging spectrometer onboard the Cheollima-2 satellite, operating in a geostationary orbit and focusing on atmospheric trace gas observations over the Asia Pacific. With a spatial resolution of 3.5 km × 8 km, it effectively monitors trace gases like HCHO and NO₂; additionally, its high temporal resolution (one regional scan per hour) captures short term dynamic changes in atmospheric composition, offering temporal insights into rapid polar photochemical processes.

The GOME-2 series (GOME-2A, GOME-2B) are onboard the sun-synchronous MetOp satellite, with an equator crossing time of 09:30 local time. They measure by receiving sunlight reflected from the Earth's atmosphere or surface, covering 240-790 nm. **Despite a relatively low**

275 spatial resolution (40 km × 40 km), they retrieve auxiliary parameters such as cloud top pressure
 276 (CTP) and effective cloud fraction via the Fast Retrieval Scheme for Clouds from the Oxygen A
 277 band (FRESCO+), supporting quality control for atmospheric composition retrieval in cloudy
 278 regions. In this study, tropospheric BrO VCD analysis uses GOME-2B products to investigate
 279 large scale polar BrO distribution.

280 Scanning Imaging Absorption Spectrometer for Atmospheric Chartography was one of the
 281 core payloads aboard the European Space Agency (ESA)'s Envisat satellite, with its operation
 282 directly tied to the satellite platform. On 8 April 2012, Envisat suffered an unexpected loss of
 283 contact; subsequently, on 9 May 2012, ESA officially declared the mission terminated, and
 284 SCIAMACHY ceased operations alongside the platform. Owing to this constraint, satellite
 285 validation of atmospheric IO observations was not performed in this study.

286 2.5 Potential Source Contribution Function

287 The PSCF is a Lagrangian receptor-oriented model employed to pinpoint potential emission
 288 source areas. For a specific grid cell (i,j), the PSCF value is defined as the ratio of the number of
 289 "polluted" trajectory endpoints ($m_{i,j}$), associated with concentrations exceeding a predefined
 290 threshold) to the total number of endpoints ($n_{i,j}$) residing in that cell.

$$291 \text{PSCF}_{i,j} = \frac{m_{i,j}}{n_{i,j}} \quad (5)$$

292 To reduce uncertainty caused by small grid counts, this study refers to Pernov et al., (2021),
 293 Polissar et al., (2001), Yin et al., (2018) by introducing a weight function to obtain the weighted
 294 PSCF (WPSCF). The formula is as follows:

$$295 \text{WPSCF}_{i,j} = W(n_{i,j}) \times \text{PSCF}_{i,j}$$

$$W(n_{i,j}) = \begin{cases} 1.00 & n_{i,j} > n_{avg} \\ 0.70 & n_{avg} / 3 < n_{i,j} \leq n_{avg} \\ 0.42 & n_{avg} / 5 < n_{i,j} \leq n_{avg} / 3 \\ 0.17 & n_{i,j} \leq n_{avg} / 5 \end{cases} \quad (6)$$

296 Where n_{avg} represents the average number of endpoints across all grid cells.

297 2.6 Auxiliary Data

298 To estimate BrO distribution, this study obtained northern hemisphere BrO data from
 299 GOME-2 products via http://www.iup.uni-bremen.de/doas/scia_data_browser.html. Sea ice
 300 concentration and age data were sourced from the National Snow and Ice Data Center.
 301 (<https://nsidc.org/home>). Chlorophyll-a concentrations were derived from Moderate Resolution
 302 Imaging Spectroradiometer (<https://aqua.nasa.gov/modis>). Backward trajectory analysis was
 303 conducted using the Hybrid Single Particle Lagrangian Integrated Trajectory model via the NASA
 304 ARL READY website to identify air mass sources. Finally, boundary layer height, wind direction,
 305 snow density, and snowfall data were obtained from the European Centre for Medium-Range
 306 Weather Forecasts (ECMWF).

307 3. Results

308 3.1 Spatial Distributions of NO₂, HCHO, BrO, and IO

309 Fig. 3 presents the spatial distributions of VCDs of four trace gases during the cruise (round
310 trip from Shanghai to the Arctic). Notably, partial data gaps exist in the cruise dataset, attributed to
311 four main interfering factors: insufficient light during nighttime navigation, spectral detection
312 interference from severe weather (e.g., thunderstorms), temporary instrument or power system
313 malfunctions, and near field data contamination by the ship's own emission plumes.

314 The high value regions of different trace gases exhibit distinct regional variations: NO₂ and
315 HCHO VCD maxima are concentrated in low latitude areas with intensive anthropogenic activities,
316 with the highest concentrations observed in the Shanghai Port region. Additionally, relatively high
317 NO₂ and HCHO concentrations are found in ports near the Korea Strait, a key shipping lane
318 connecting the Pacific Ocean and the Sea of Japan, frequented by international merchant vessels.
319 The elevated pollutant levels in these regions are likely directly linked to ship emissions from port
320 operations and shipping lanes, a mechanism supported by numerous previous studies (Hwang and
321 Kang, 2023; Wang et al., 2018). In contrast, high VCDs of the reactive halogen species IO and
322 BrO are concentrated in the Arctic Ocean. The maximum BrO VCD is observed near the Arctic
323 Beaufort Sea, while the maximum IO VCD occurs near the Arctic Bering Strait.

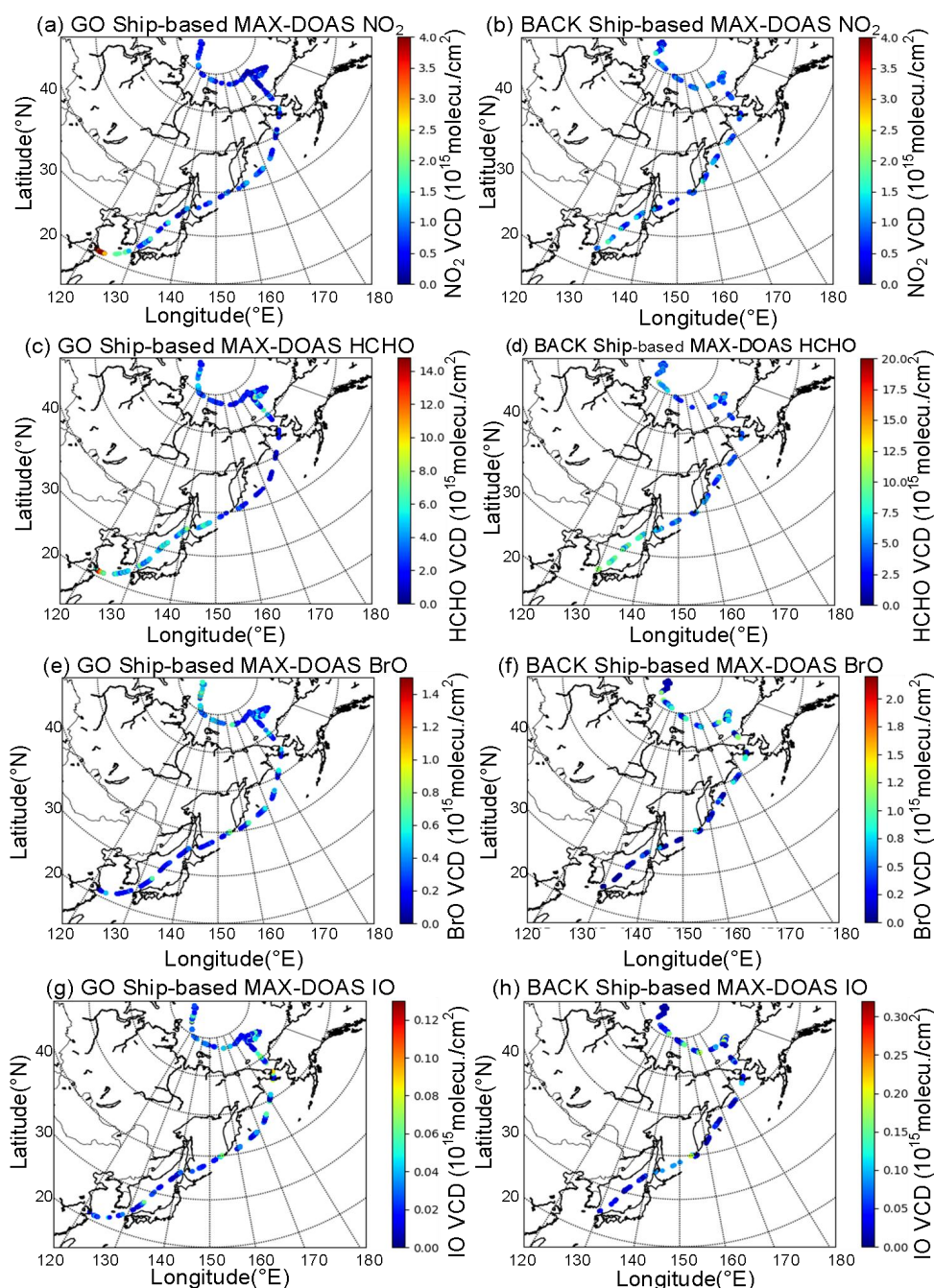
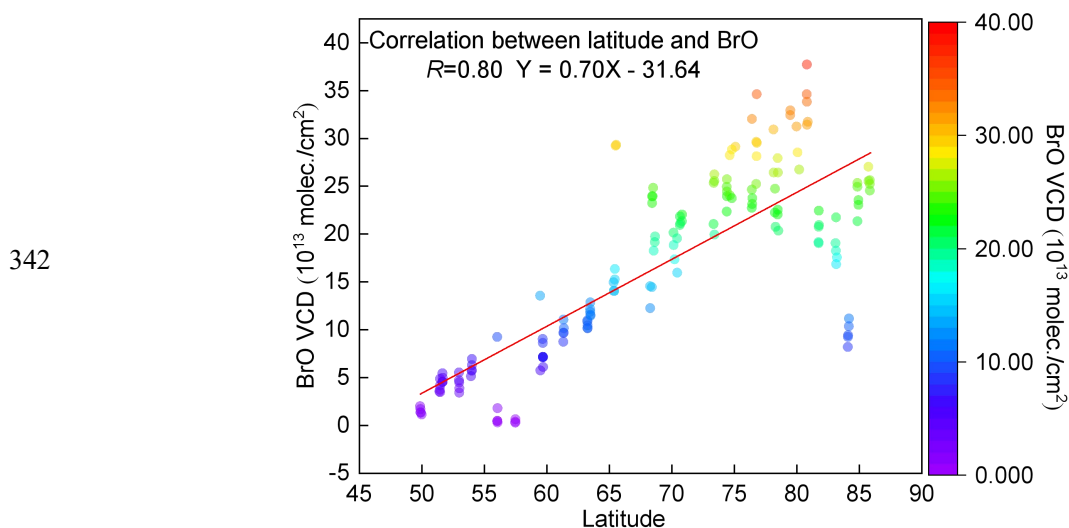


Fig. 3. Spatial distributions of trace gases (NO_2 , HCHO, BrO, and IO) VCDs.

Panels (a), (c), (e), (g) present NO_2 , HCHO, BrO, and IO distributions along the go route from Shanghai to the Arctic, while panels (b), (d), (f), (h) show their distributions along the return route from the Arctic to Shanghai.

Fig. 3 shows that BrO concentrations generally increase with latitude. Previous studies (Simpson et al., 2007; Zhao et al., 2016) have identified high latitude Northern Hemisphere regions as cores of abnormally elevated tropospheric BrO, with these high values typically linked to key physicochemical mechanisms: sea ice photochemical processes (e.g., bromine explosion) and low temperature catalysis. Thus, this study focuses on data at and north of 50°N . Data were analyzed at 1° latitude intervals, selecting the top 5 BrO concentrations and their corresponding

335 latitude information per interval. As shown in Fig. 4, BrO concentrations exhibit a positive
336 correlation with latitude, with a correlation coefficient of 0.80. In contrast, IO spatial distribution
337 shows no distinct latitudinal gradient, suggesting its concentrations are more strongly associated
338 with the spatial heterogeneity of marine biological activities (e.g., phytoplankton emissions). **The**
339 **relationship between IO and chlorophyll-a concentrations will be analyzed in depth in subsequent**
340 **sections, incorporating synchronously observed marine ecological data (see Section 3.3.1 for**
341 **details).**

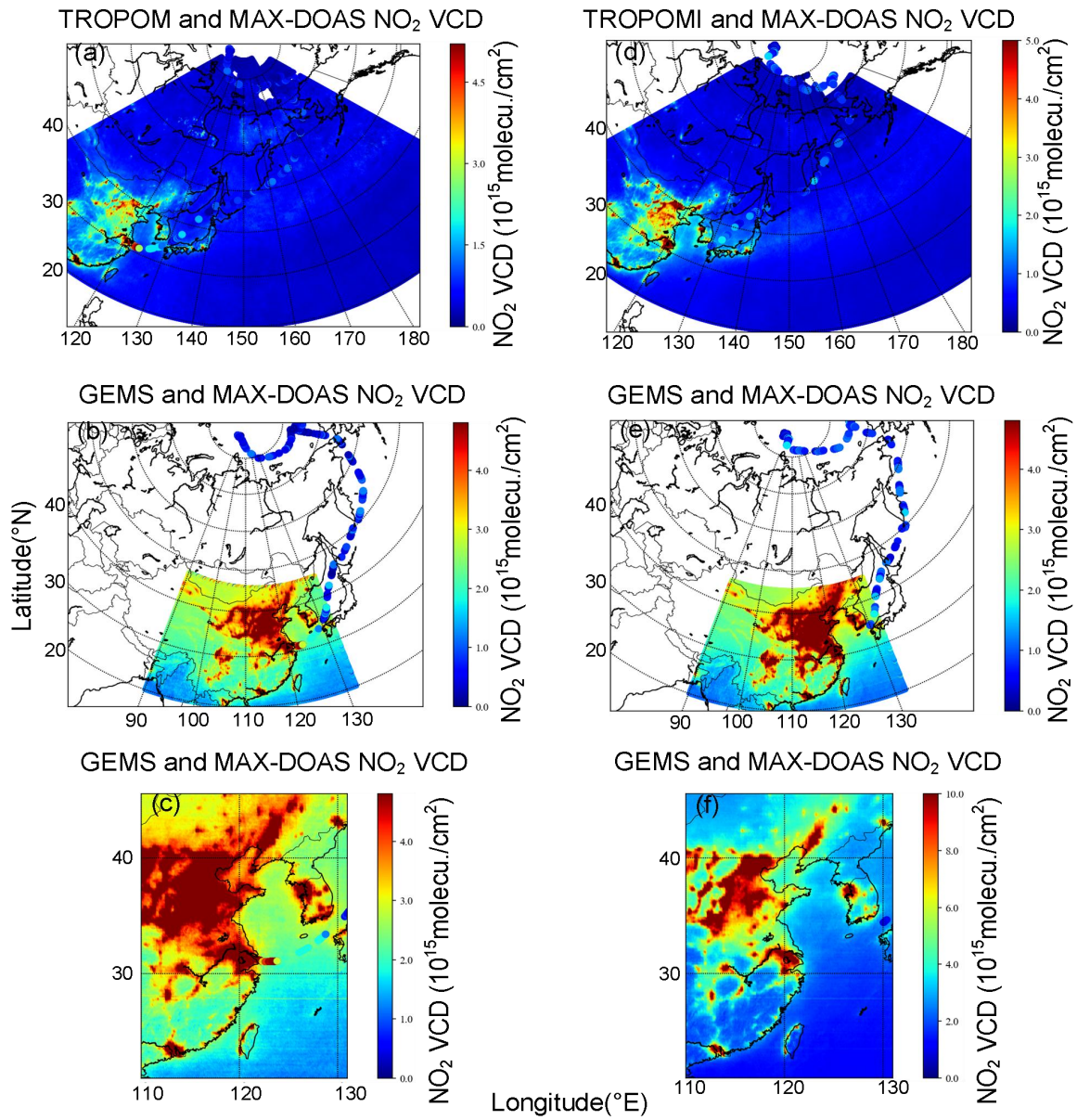


343 **Fig. 4.** BrO concentration variation observed by ship-based MAX-DOAS with latitude

344 **3.2 Satellite Comparison**

345 Ship-based MAX-DOAS measured NO_2 , HCHO, and BrO VCDs were compared with
346 atmospheric products from GEMS, TROPOMI, and GOME-2 satellites to validate the
347 applicability of satellite data in the Arctic and adjacent seas. Results are presented in Fig. 5 (NO_2),
348 Fig. 6 (HCHO), and Fig. 7 (BrO).

349 **To ensure data reliability, satellite products with high cloud contamination (effective cloud**
350 **fraction > 0.4) and poor retrieval quality (relative error > 100%) were excluded. This filtering is**
351 **necessary because cloud particles significantly interfere with ultraviolet-visible radiation**
352 **transmission, altering the optical path length and leading to biases in trace gas retrieval.** Qualified
353 satellite data were temporally averaged (matching the temporal resolution of ship-based
354 observations) and interpolated to $0.1^\circ \times 0.1^\circ$ gridded data using a parabolic spline interpolation
355 algorithm (Chan et al., 2015, 2018; Kuhlmann et al., 2014). **This gridding process not only**
356 **preserves the true spatial distribution of trace gases but also retains details of pollution hotspots**
357 **(e.g., ports, shipping lanes), avoiding comparison biases from spatial scale mismatch** (Hong et al.,
358 2018). Since GEMS is focused on the Asia Pacific region and its effective detection boundary
359 does not cover high latitude Arctic areas, it was only used for comparison within $110^\circ E$ - $130^\circ E$,
360 $20^\circ N$ - $45^\circ N$ to ensure spatial coverage consistency with ship-based observations.



361

362

363

364

Fig. 5. Comparison of ship-based MAX-DOAS measured NO₂ VCDs with satellite observations: (a-c) Shanghai to Arctic and (d-f) Arctic to Shanghai.

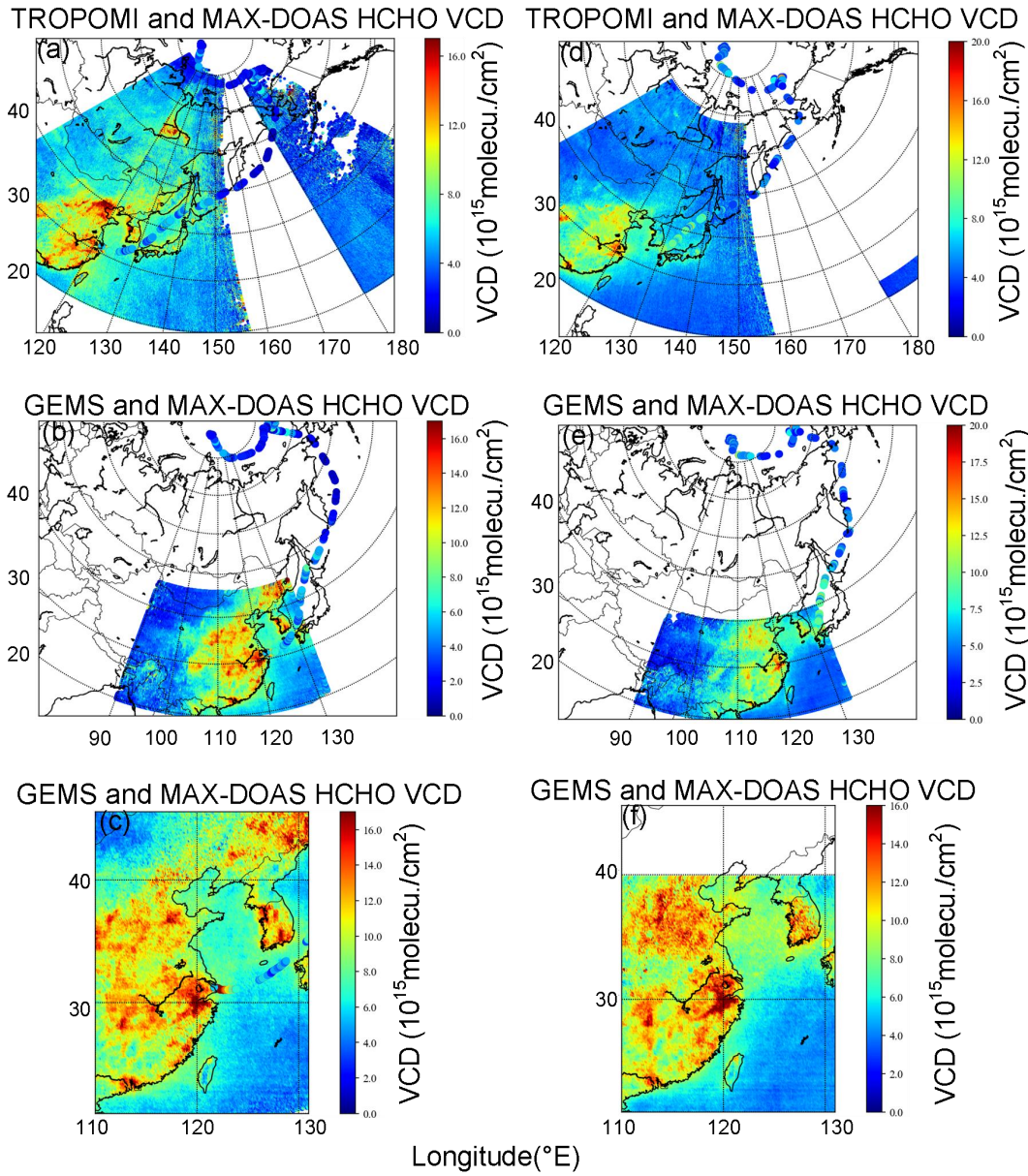


Fig. 6. Comparison of ship-based MAX-DOAS measured HCHO VCDs with satellite observations: (a-c) Shanghai to Arctic and (d-f) Arctic to Shanghai.

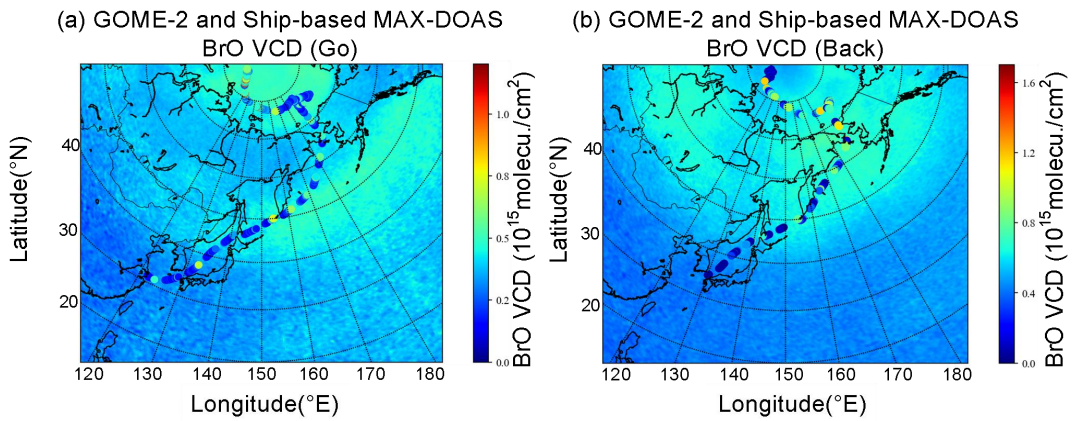
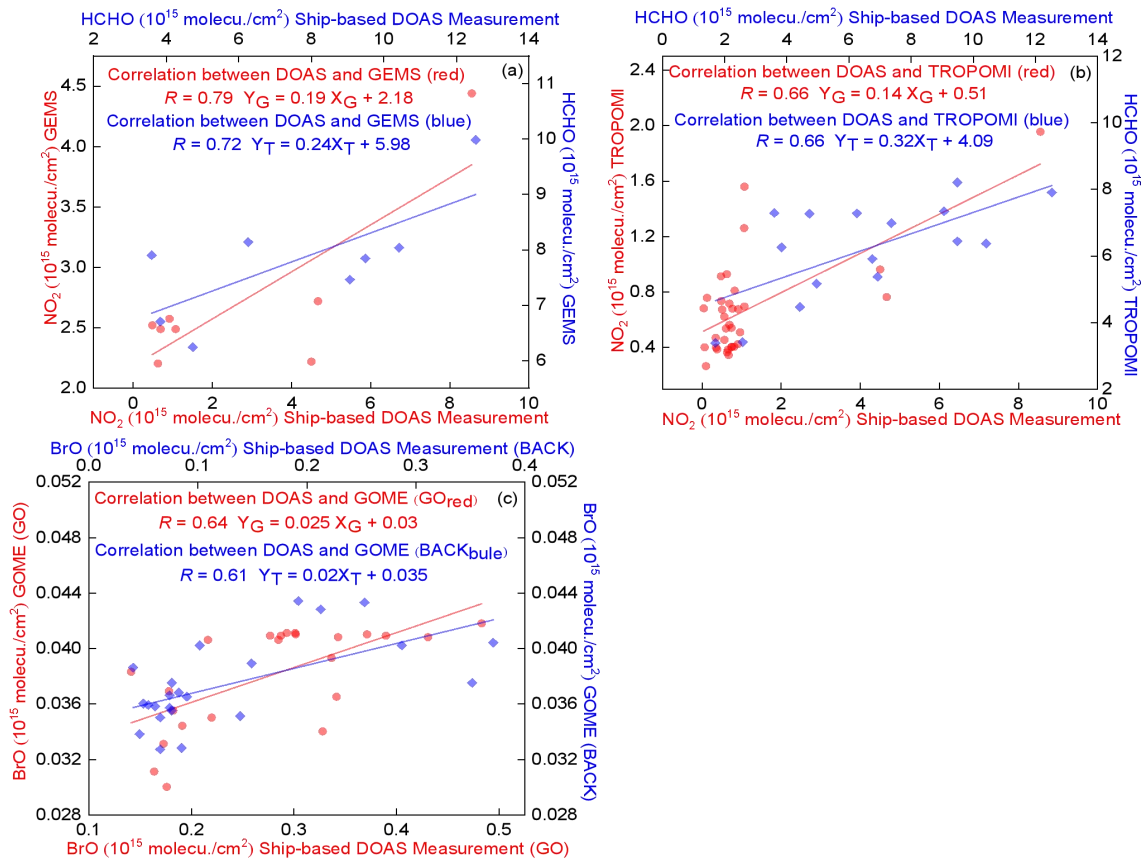


Fig. 7. Comparison of ship-based MAX-DOAS measured BrO VCDs with GOME-2 observations: (a) Shanghai to Arctic and (b) Arctic to Shanghai.

372 Direct comparisons in Figs. 5-7 reveal good overall consistency between ship-based
 373 MAX-DOAS and satellite observations (TROPOMI, GEMS, GOME-2). Notably, in mid-to-low
 374 latitude marine regions (e.g., Shanghai Port, Korea Strait), the spatial localization of HCHO and
 375 NO₂ high value areas is consistent. In Arctic regions (e.g., Beaufort Sea, Bering Strait), BrO
 376 concentration trends also exhibit clear coherence. To further quantify this consistency, satellite
 377 data were gridded and averaged over daily mobile measurement areas. Correlation analysis was
 378 performed between daily mean satellite values and daily mean mobile MAX-DOAS values
 379 throughout the cruise, with results shown in Fig. 8 (a)-(c).



380
 381
 382 **Fig. 8.** Correlation analysis between daily measurements and satellite observations during the
 383 ship-based campaign. Panels (a) GEMS, (b) TROPOMI, (c) GOME-2.

384 Ship-based MAX-DOAS measured NO₂ and HCHO VCDs exhibit correlation coefficients of
 385 0.79 and 0.72 with GEMS satellite observations, respectively, and 0.66 for both species with
 386 TROPOMI observations. For BrO VCDs from round trip ship-based measurements, correlations
 387 with GOME-2 are 0.64 (go) and 0.61 (back). Notably, the GEMS correlation analysis uses a
 388 relatively small sample size (constrained by its observation coverage). **To rule out the confounding**
 389 **effect of high correlation due to small sample size, TROPOMI data of the same sample size as**
 390 **GEMS were selected within 110°E-130°E, 20°N-45°N for recalculation (see Fig. S4).** The
 391 correlation coefficient between ship-based NO₂ VCDs and TROPOMI rose to 0.73, whereas that

392 for HCHO VCDs dropped to 0.20. This result further verifies that the strong correlation between
393 GEMS and ship-based observations does not stem from data volume deviation, but is most likely
394 closely linked to GEMS' higher temporal resolution (1 observation per hour). In contrast to
395 TROPOMI's daily observational frequency, GEMS more accurately matches the temporal
396 dynamics of ship-based MAX-DOAS measurements, mitigating concentration biases induced by
397 time period discrepancies.

398 Discrepancies between ship-based MAX-DOAS and satellite observations arise primarily
399 from three factors: 1). **Satellites have substantially lower spatial resolution than ship-based**
400 **MAX-DOAS point scale measurements and are less sensitive to local trace gas sources** (e.g.,
401 transient ship emissions). In contrast, ship-based MAX-DOAS exhibits higher sensitivity to the
402 lower atmosphere, enabling precise capture of short-term emission signals from near sea surface
403 pollutants (Wu et al., 2018). **This leads to slightly higher ship-based observations compared to**
404 **satellite retrievals in trace gas intensive regions (e.g., ports, shipping lanes)**. 2). Satellite retrievals
405 are vulnerable to aerosols and clouds in the Arctic and adjacent seas. Even with cloud fraction
406 screening, cloud particles can modify radiative transfer paths, resulting in underestimated trace gas
407 absorption signals. ship-based MAX-DOAS, however, partially mitigates aerosol scattering
408 interference through multi-azimuth observations, delivering more stable measurements. 3). VCDs
409 from both platforms require conversion using the AMF. AMF calculations integrate multiple
410 variables: trace gas profiles, aerosol profiles, and surface albedo. Variations in calculation
411 assumptions thus induce VCD discrepancies.

412 **3.3 Sources of Reactive Halogen Species in the Arctic**

413 **BrO and IO are core trace gases in polar atmospheric chemistry, but their emission pathways**
414 **and driving mechanisms show significant differences. BrO concentrations are typically influenced**
415 **by the coupling of physicochemical and meteorological factors, specifically the "bromine**
416 **explosion cycle," which involves complex heterogeneous reactions on various saline interfaces. In**
417 **contrast, IO in the Arctic boundary layer is mainly related to direct emissions from marine**
418 **biogenic sources. Therefore, this section adopts a multi-factor synergistic analysis to resolve the**
419 **drivers of BrO. The analysis for IO focuses on its biogenic driving attributes, emphasizing the**
420 **influence of biological activity, represented by chlorophyll-a, on boundary layer IO**
421 **concentrations.**

422 **3.3.1 Drivers and Modulating Factors of Arctic BrO**

423 To clarify the primary sources of BrO and their coupling with sea ice, this study integrated
424 satellite remote sensing data and NSIDC sea ice concentration to analyze the spatiotemporal
425 distribution of Arctic sea-ice from July to September 2021 (see Fig. S5). The results showed that
426 sea-ice was in the summer ablation phase in August: dense ice was concentrated in the central
427 Arctic Ocean and its periphery, with significant retreat of the sea ice edge zone. This
428 spatiotemporal sea ice pattern provides a basis for subsequent analyses of air mass sea ice contact

429 duration and the characteristics of the sea ice edge zone in BrO source regions. Subsequently,
430 backward trajectory analysis was performed using the HYSPLIT model to focus on the regulatory
431 effects of air mass transport paths and sea ice contact duration on reactive halogen concentrations,
432 and to quantify the impact of transport processes on source contributions. Observational data from
433 the Xuelong research vessel in the high latitude dense Arctic ice zone (August 6-30, 2021) were
434 used, with the frequently monitored representative site (86.40°N, 86.0°E) as the target location.
435 Backward trajectories were calculated every 6 hours (cutoff time: 19:00 UTC on August 30), and
436 air mass movements were simulated at three altitudes (0 m, 500 m, 1000 m) to characterize
437 transport properties at different boundary layer heights. Backward trajectory results during the
438 ship-based MAX-DOAS campaign are presented in Supplementary Fig. S6. Sea ice contact
439 duration $T(t, h)$ is defined as the cumulative time that an air mass arriving at the target location at
440 time t and height h remains above sea ice and below the threshold height z_0 . Following previous
441 studies (Frieß et al., 2004), z_0 was set to 200 m within the boundary layer's near surface mixing
442 layer, where air undergoes sufficient exchange with the sea ice surface. This facilitates BrO
443 formation via absorption of reactive bromine or sea salt aerosols (Choi et al., 2018; Jozef et al.,
444 2024; McPhee, 2017).

445 Fig. S7 was plotted backward trajectories from the Xuelong 2 research cruise on NSIDC sea
446 ice concentration data (August 2021), with different colored curves representing air mass
447 trajectories at 0 m, 500 m, and 1000 m altitudes. Sea ice contact durations of the polluted air
448 masses were calculated using the predefined threshold height, yielding values of 30 h, 42 h, 25 h,
449 and 18 h for the dates shown in the figure. With this methodological framework established,
450 GOME-2 satellite retrievals were used to derive the average BrO VCD distribution in the Arctic
451 and adjacent seas (July-September 2021; Fig. 9a). BrO concentrations exhibit a zonal gradient
452 centered on the polar region: high values are concentrated in the sea ice edge zone north of 50°N
453 and the central Arctic Ocean, while concentrations are significantly lower in mid-to-low latitudes
454 south of 50°N. This distribution aligns with the classic mechanism: brine layers on sea ice surfaces
455 or beneath snow cover provide critical reaction interfaces for the photochemical activation of
456 halides (e.g., NaCl), facilitating the multi-step conversion of bromide ions (Br^-) to gaseous BrO
457 (Begoin et al., 2010; Saiz-Lopez et al., 2008). To validate the link between source regions and
458 latitude, the latitudinal variation of BrO concentrations (July-September) was plotted (see Fig. S8).
459 **BrO concentrations generally increase with latitude but slightly decrease in the near polar central**
460 **region (above 85°N). This phenomenon is consistent with the conclusion of Begoin et al. (2010)**
461 **that Arctic BrO high values are concentrated in the sea ice edge zone.** This is presumably due to
462 lower halide activation efficiency in the fully ice-covered central Arctic compared to the sea ice
463 edge zone, coupled with enhanced photochemical consumption of BrO, resulting in lower
464 concentrations (Chen et al., 2023).

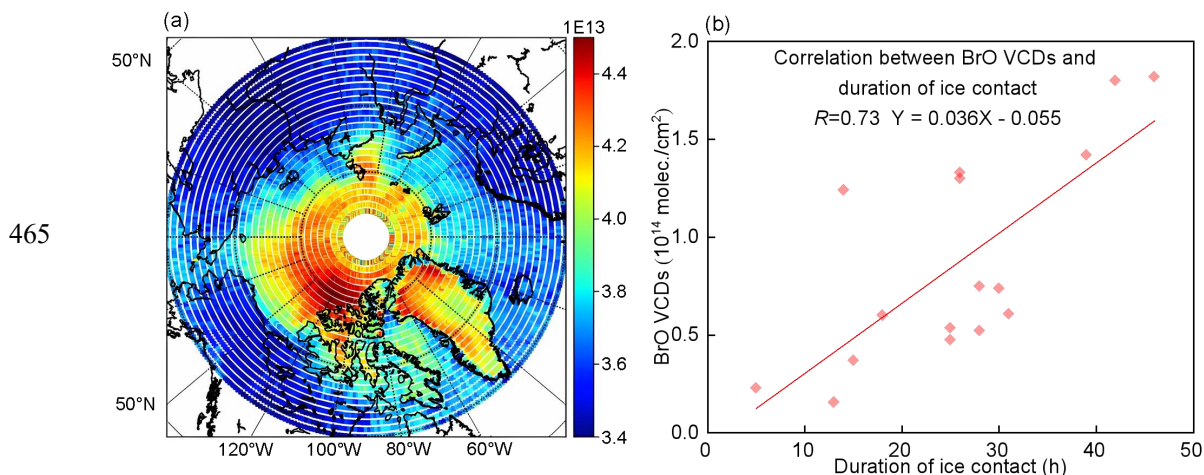


Fig. 9. Source region characteristics of Arctic BrO. (a) GOME-2 derived spatial distribution of BrO VCDs. (b) Correlation between air mass sea ice contact duration and ship-based BrO VCDs

To further validate source region characteristics, this study integrated satellite observed BrO spatial distributions with ship-based MAX-DOAS observations. Maximum daily BrO VCDs from ship-based measurements were paired with their corresponding air mass sea ice contact durations, and correlation analysis was performed (Fig. 9b). The two variables exhibit a positive correlation ($R=0.73$), consistent with the findings of Wagner et al. (2007). This indicates that the longer air masses reside over sea ice, the higher the likelihood of absorbing halides from sea ice and participating in bromine explosion events ultimately increasing BrO concentrations at the observation site (Wagner et al., 2007). This finding also explains the satellite observed pattern: BrO maxima are concentrated in the sea ice edge zone rather than the fully ice-covered central Arctic. This is attributed to intense dynamic changes in the sea ice edge zone, which enhance halide activation efficiency, and air mass transport paths in these regions are more likely to satisfy the condition of prolonged sea ice contact (Cao et al., 2024).

To elucidate the synergistic impacts of environmental parameters and quantify their respective contributions to bromine activation, we employed a Generalized Additive Model (GAM) to investigate BrO variability (see Supplement Fig. S9). The model achieved an overall correlation of $R = 0.80$. Our quantitative assessment identifies sea-ice contact time as the primary driver of BrO enhancements, accounting for an independent contribution of 48.63%. This finding statistically verifies that surface contact is the fundamental requirement for bromine activation and subsequent accumulation. Snowfall contributes 8.81% to the variance, where its negative correlation reflects the physical masking of saline source regions (e.g., frost flowers or salty snowpacks) by fresh snow, thereby inhibiting heterogeneous chemical reactions. While the direct contributions from wind direction (3.77%) and boundary layer height (3.42%) are modest, comparative sub-group analysis (e.g., $R = 0.87$ for snow-free periods versus $R = 0.61$ during snowfall) indicates that meteorological forcing primarily governs the intensity and efficiency of "bromine explosions" by modulating boundary layer stability and air mass trajectories (Bognar et

494 al., 2020). The remaining unexplained variance (35.37%) is likely associated with environmental
495 drivers not captured in the current model. Comprehensive details concerning how environmental
496 parameters modulate the relationship between BrO abundances and sea-ice contact duration are
497 available in the Supplement Fig. S10 -Fig. S17.

498 Using backward trajectory data, this study performed PSCF analysis to identify BrO's
499 potential source regions and quantify their contributions to BrO concentrations at the observation
500 site (Fig. 10). To pinpoint core potential source regions, high BrO concentrations (threshold:
501 6.0×10^{13} molec./cm²) from ship-based MAX-DOAS observations were used as the benchmark.
502 PSCF results indicate that high probability potential BrO sources are concentrated in western
503 Greenland, the seas north of North America, and the Arctic sea-ice edge zone. Sea ice dynamic
504 processes in these regions, including halide release from sea ice melting and sea salt aerosol
505 formation and transport enhance bromine activation efficiency, making them the primary
506 contributors to BrO at the observation site (Cao et al., 2024; Jozef et al., 2024) This aligns with the
507 satellite-observed source region characteristics in Section 3.3.1, further confirming that sea ice is
508 BrO's core source.

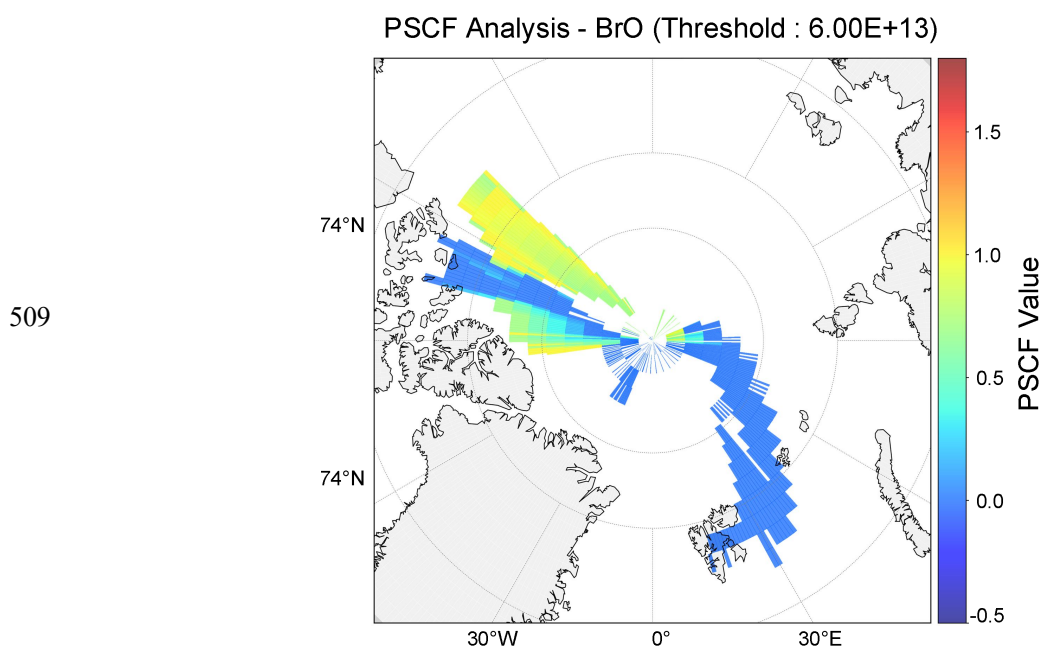


Fig. 10. PSCF analysis for BrO in the Arctic

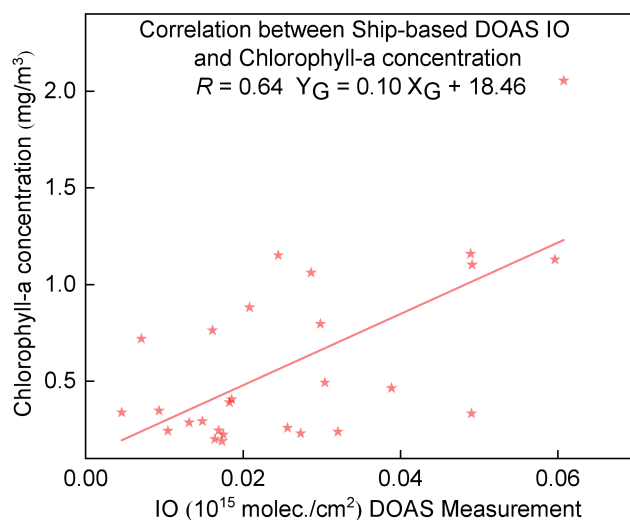
3.3.2 Biogenic Sources of IO: Coupling with Chlorophyll-a Concentration

513 To address IO's sources, this study focused on its link to marine biological processes. Using
514 chlorophyll-a, which is a key indicator of phytoplankton biomass, as a proxy, we integrated
515 MODIS satellite data, ship-based observations, and backward trajectory data to assess IO's
516 biogenic source contributions from two dimensions: spatial distribution coupling and quantitative
517 concentration correlation. First, chlorophyll-a concentration spatial distribution (July-September
518 2021) was retrieved from MODIS satellite data (see Fig. S18). The results show that high

519 chlorophyll-a concentrations are concentrated in coastal regions, with particularly prominent
520 signals in the Bering Strait and its vicinity. This reflects significant phytoplankton biomass
521 accumulation in the area during late summer and early autumn (Grebmeier et al., 2006), providing
522 a potential site for biogenic iodine enrichment.

523 To further verify the spatial association between high IO air masses and phytoplankton
524 enriched regions, backward trajectories of air masses during high IO concentration periods
525 (Xuelong 2 cruise) were overlaid on MODIS chlorophyll-a concentration data (August 2021; see
526 Fig. S19). The results indicate that trajectories of high-probability IO sources extensively cover
527 chlorophyll-a hotspots, including the Bering Strait, southern Greenland, and coastal North Atlantic
528 waters. This directly confirms the spatial coupling between phytoplankton biological processes
529 and IO formation in these regions. Building on this spatial correlation and previous research,
530 phytoplankton enrich iodine in seawater via biological processes (e.g., cellular metabolism, death
531 and decomposition) and release iodine species across the sea-water-atmosphere interface (or sea
532 ice brine channels). These iodine species then participate in the photochemical production of IO
533 (Saiz-Lopez et al., 2015).

534 To quantify the relationship between ship-based MAX-DOAS measured IO VCDs and
535 chlorophyll-a concentrations, MODIS chlorophyll-a data were averaged over a $0.1^\circ \times 0.1^\circ$ grid
536 within the daily coverage of ship-based IO observations. Correlation analysis with daily average
537 IO VCDs yielded a moderate positive correlation ($R=0.64$; Fig. 11), confirming biogenic sources
538 as an important contributor to IO. Factors contributing to the relatively weak correlation may
539 include: Satellite observational constraints: MODIS cannot detect phytoplankton communities
540 within and beneath sea ice, where the under-ice light environment and nutrient availability still
541 support phytoplankton growth. This leads to incomplete characterization of biogenic iodine
542 potential by chlorophyll-a retrievals (Saiz-Lopez et al., 2015); Confounding abiotic processes: IO
543 concentrations are also influenced by sea ice melting (which releases inorganic iodine) and
544 photochemical oxidation (which regulates iodine species transformation), weakening the
545 correlation with chlorophyll-a (Saiz-Lopez et al., 2015).

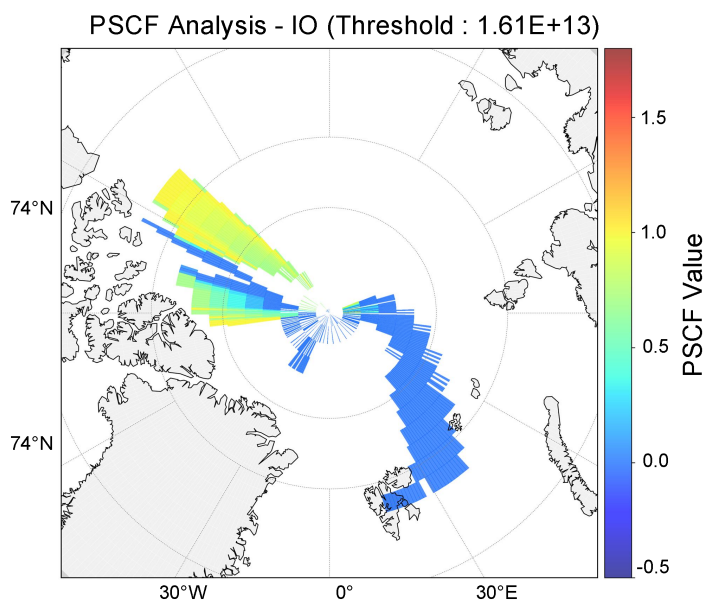


546

547 **Fig. 11.** Correlation between ship-based IO VCDs and Chlorophyll-a

548

549 Using backward trajectory data, PSCF analysis was performed to identify IO's potential
 550 source regions and quantify their contributions to IO concentrations at the observation site (Fig.
 551 12). To delineate these source regions, ship-based high IO concentrations (threshold: 1.61×10^{13}
 552 molec./cm²) were used as the benchmark. High probability potential IO sources are similar to
 553 those of BrO, concentrated in western Greenland, the seas north of North America, and the Arctic
 554 sea-ice edge zone. These regions likely support high phytoplankton biomass: phytoplankton enrich
 555 iodine in seawater via metabolic processes and release iodine species to the atmosphere through
 556 sea-water-atmosphere interface exchange. These species then participate in the photochemical
 production of reactive iodine compounds (Mahajan et al., 2021).



557

558

559 **Fig. 12.** PSCF analysis for IO in the Arctic

560

561 Comparison of BrO and IO PSCF results reveals spatial differences in their potential source
 regions: BrO sources are concentrated in high latitude sea-ice-covered areas, while IO sources are
 centered in mid-to-low latitude coastal biologically active zones. In addition, correlation analysis

562 of ship-based BrO and IO VCDs (see Fig. S20) yielded a correlation coefficient $R=0.5$, indicating
563 a moderate association between the two. This result is reasonably explained by the PSCF
564 identified source region characteristics: Arctic BrO and IO derive from a shared
565 ice-sea-atmosphere exchange environment (e.g., material exchange interfaces in the sea ice edge
566 zone), which provides a basis for their correlation (Giesse et al., 2021; McFiggans et al., 2000;
567 Saiz-Lopez et al., 2015); The distinct source biases revealed by PSCF, namely BrO's dominance of
568 sea ice sources and IO's reliance on biogenic sources, result in a relatively weak correlation.
569

570 4. Conclusion

571 This study presents the spatial distributions of trace gases (NO_2 , HCHO, BrO, and IO)
572 captured during the 12th Chinese Arctic Scientific Expedition (July - September 2021) along a
573 transect from Shanghai to the Arctic. Utilizing ship-based Multi-Axis Differential Optical
574 Absorption Spectroscopy (MAX-DOAS), we establish a robust ground-truth baseline to assess the
575 performance of TROPOMI, GEMS, and GOME-2 satellite products in polar regions. Statistical
576 analyses yield correlation coefficients between 0.61 and 0.79, validating the efficacy of satellite
577 remote sensing for monitoring atmospheric composition over the Arctic and adjacent oceans. Our
578 findings demonstrate that tropospheric BrO is primarily controlled by Sea Ice Contact (SIC)
579 duration, which accounts for 48.63% of the variance in a GAM. Potential BrO source regions are
580 identified in western Greenland, the high-latitude Canadian Arctic, and the Marginal Ice Zone
581 (MIZ). The R value between BrO and SIC improved from 0.73 to 0.77 after incorporating
582 dynamic boundary layer height (BLH) constraints. Furthermore, meteorological conditions
583 significantly modulate bromine activation: southwesterly winds enhanced the correlation to 0.84,
584 whereas snowfall weakened it from 0.87 to 0.61. In contrast to the complex physico-chemical
585 regulation of BrO, IO variability is predominantly driven by biogenic emissions, correlating
586 strongly with chlorophyll-a ($R=0.64$), particularly in phytoplankton-rich regions like the Bering
587 Strait. Notably, we observe a distinct spatial divergence between the source regions of
588 sea-ice-driven BrO and biogenic IO. However, a moderate correlation ($R=0.5$) persists within the
589 MIZ, suggesting that the ice-ocean-atmosphere interface facilitates shared precursors or formation
590 pathways for these reactive halogens. In conclusion, this study provides high-precision validation
591 for Arctic satellite retrievals and systematically characterizes the drivers of polar halogen species.
592 These data offer critical constraints for optimizing emission parameterizations and halogen budget
593 accounting in chemical transport models, such as GEOS-Chem and WRF-Chem.
594

595 **Data availability.** All measurement data used in this study are publicly available at Zenodo via
596 the permanent DOI: <https://doi.org/10.5281/zenodo.18072720>. Additionally, they can also be
597 made available for scientific purposes upon request to the authors (Cheng Liu,
598 chliu81@ustc.edu.cn, and Chengzhi Xing, xingcz@aiofm.ac.cn).
599

600 **Author contributions.** QZ, CX and CL (Cheng Liu) designed the research and organized the

601 paper. QZ wrote the paper, while CX and CL (Cheng Liu) edited it. QZ, CX, YL, HP, WT, HL, CL
602 (Chao Liu), ZZ, WM and TT contributed to the retrieval of DOAS data and satellite data. QZ, CX,
603 YL, HP, WT, HL, CL (Chao Liu), ZZ, WM and TT contributed to data analysis. All the
604 above-mentioned authors contributed to the revision of the paper.

605
606 **Competing interests.** The contact author has declared that none of the authors has any
607 competing interests.

608
609 **Acknowledgements.** We would like to thank Zhouqing Xie's group for effectively organizing
610 the observation. We thank the National Oceanic and Atmospheric Administration (NOAA) Air
611 Resources Laboratory (ARL) for providing the open HYSPLIT transport and dispersion model.

612
613 **Financial support.** This study was supported by the National Natural Science Foundation of
614 China (grant nos. 42225504 and U21A2027), the President's Foundation of Hefei Institutes of
615 Physical Science, Chinese Academy of Sciences (grant no. BJPY2024B09, YZJJQY202401).

616 617 **Reference**

618 Adachi, K., Tobo, Y., Koike, M., Freitas, G., Zieger, P., and Krejci, R.: Composition and mixing
619 state of Arctic aerosol and cloud residual particles from long-term single-particle observations at
620 Zeppelin Observatory, Svalbard, *Atmospheric Chemistry and Physics*, 22, 14421-14439,
621 <https://doi.org/10.5194/acp-22-14421-2022>, 2022.

622 Begoin, M., Richter, A., Weber, M., Kaleschke, L., Tian-Kunze, X., Stohl, A., Theys, N., and
623 Burrows, J. P.: Satellite observations of long-range transport of a large BrO plume in the Arctic,
624 *Atmospheric Chemistry and Physics*, 10, 6515-6526, <https://doi.org/10.5194/acp-10-6515-2010>,
625 2010.

626 Behrens, L. K., Hilboll, A., Richter, A., Peters, E., Alvarado, L. M. A., Kalisz Hedegaard, A. B.,
627 Wittrock, F., Burrows, J. P., and Vrekoussis, M.: Detection of outflow of formaldehyde and
628 glyoxal from the African continent to the Atlantic Ocean with a MAX-DOAS instrument,
629 *Atmospheric Chemistry and Physics*, 19, 10257-10278,
630 <https://doi.org/10.5194/acp-19-10257-2019>, 2019.

631 Blechschmidt, A.-M., Richter, A., Burrows, J. P., Kaleschke, L., Strong, K., Theys, N., Weber, M.,
632 Zhao, X., and Zien, A.: An exemplary case of a bromine explosion event linked to cyclone
633 development in the Arctic, *Atmospheric Chemistry and Physics*, 16, 1773-1788,
634 <https://doi.org/10.5194/acp-16-1773-2016>, 2016.

635 Bloss, W. J., Lee, J. D., Johnson, G. P., Sommariva, R., Heard, D. E., Saiz-Lopez, A., Plane, J. M.
636 C., McFiggans, G., Coe, H., Flynn, M., Williams, P., Rickard, A. R., and Fleming, Z. L.: Impact of
637 halogen monoxide chemistry upon boundary layer OH and HO₂ concentrations at a coastal site,
638 *Geophysical Research Letters*, 32, <https://doi.org/10.1029/2004GL022084>, 2005.

639 Bogner, K., Zhao, X., Strong, K., Chang, R. Y. W., Frieß, U., Hayes, P. L., McClure-Begley, A.,
640 Morris, S., Tremblay, S., and Vicente-Luis, A.: Measurements of Tropospheric Bromine Monoxide

641 Over Four Halogen Activation Seasons in the Canadian High Arctic, *Journal of Geophysical*
642 *Research: Atmospheres*, 125, e2020JD033015, <https://doi.org/10.1029/2020JD033015>, 2020.

643 Bougoudis, I., Blechschmidt, A.-M., Richter, A., Seo, S., Burrows, J. P., Theys, N., and Rinke, A.:
644 Long-term time series of Arctic tropospheric BrO derived from UV-VIS satellite remote sensing
645 and its relation to first-year sea ice, *Atmospheric Chemistry and Physics*, 20, 11869-11892,
646 <https://doi.org/10.5194/acp-20-11869-2020>, 2020.

647 Brockway, N., Peterson, P. K., Bigge, K., Hajny, K. D., Shepson, P. B., Pratt, K. A., Fuentes, J. D.,
648 Starn, T., Kaeser, R., Stirm, B. H., and Simpson, W. R.: Tropospheric bromine monoxide vertical
649 profiles retrieved across the Alaskan Arctic in springtime, *Atmospheric Chemistry and Physics*, 24,
650 23-40, <https://doi.org/10.5194/acp-24-23-2024>, 2024.

651 Cao, Y., Wang, Z., Liu, J., Ma, Q., Li, S., Liu, J., Li, H., Zhang, P., Chen, T., Wang, Y., Chu, B.,
652 Zhang, X., Saiz-Lopez, A., Francisco, J. S., and He, H.: Spontaneous Molecular Bromine
653 Production in Sea-Salt Aerosols, *Angewandte Chemie International Edition*,
654 <https://doi.org/10.1002/anie.202409779>, 2024.

655 Carlos Gómez Martín, J., Spietz, P., and Burrows, J. P.: Spectroscopic studies of the I₂/O₃
656 photochemistry, *Journal of Photochemistry and Photobiology A: Chemistry*, 176, 15-38,
657 <https://doi.org/10.1016/j.jphotochem.2005.09.024>, 2005.

658 Chan, K. L., Hartl, A., Lam, Y. F., Xie, P. H., Liu, W. Q., Cheung, H. M., Lampel, J., Poehler, D.,
659 Li, A., and Xu, J.: Observations of tropospheric NO₂ using ground-based MAX-DOAS and OMI
660 measurements during the Shanghai World Expo 2010, *Atmospheric Environment*, 119, 45-58,
661 <https://doi.org/10.1016/j.atmosenv.2015.08.041>, 2015.

662 Chan, K. L., Wiegner, M., Wenig, M., and Pöhler, D.: Observations of tropospheric aerosols and
663 NO₂ in Hong Kong over 5 years using ground-based MAX-DOAS, *Science of the Total*
664 *Environment*, 619-620, 1545-1556, <https://doi.org/10.1016/j.scitotenv.2017.10.153>, 2018.

665 Chance, K. V. and Spurr, R. J. D.: Ring effect studies: Rayleigh scattering, including molecular
666 parameters for rotational Raman scattering, and the Fraunhofer spectrum, *Applied Optics*, AO, 36,
667 5224-5230, <https://doi.org/10.1364/AO.36.005224>, 1997.

668 Chen, Y., Liu, S., Zhu, L., Seo, S., Richter, A., Li, X., Ding, A., Sun, W., Shu, L., Wang, X., Valks,
669 P., Hendrick, F., Koenig, T. K., Volkamer, R., Bai, B., Wang, D., Pu, D., Sun, S., Li, J., Zuo, X., Fu,
670 W., Li, Y., Zhang, P., Yang, X., and Fu, T. M.: Global Observations of Tropospheric Bromine
671 Monoxide (BrO) Columns From TROPOMI, *Journal of Geophysical Research: Atmospheres*, 128,
672 e2023JD039091, <https://doi.org/10.1029/2023JD039091>, 2023.

673 Choi, S., Theys, N., Salawitch, R. J., Wales, P. A., Joiner, J., Canty, T. P., Chance, K., Suleiman, R.
674 M., Palm, S. P., Cullather, R. I., Darmenov, A. S., da Silva, A., Kurosu, T. P., Hendrick, F., and Van
675 Roozendaal, M.: Link Between Arctic Tropospheric BrO Explosion Observed From Space and
676 Sea-Salt Aerosols From Blowing Snow Investigated Using Ozone Monitoring Instrument BrO
677 Data and GEOS-5 Data Assimilation System, *Journal of Geophysical Research: Atmospheres*, 123,

678 6954-6983, <https://doi.org/10.1029/2017JD026889>, 2018.

679 Čížková, K., Láska, K., Metelka, L., and Staněk, M.: Assessment of spectral UV radiation at
680 Marambio Base, Antarctic Peninsula, *Atmospheric Chemistry and Physics*, 23, 4617-4636,
681 <https://doi.org/10.5194/acp-23-4617-2023>, 2023.

682 Coburn, S., Dix, B., Sinreich, R., and Volkamer, R.: The CU ground MAX-DOAS instrument:
683 characterization of RMS noise limitations and first measurements near Pensacola, FL of BrO, IO,
684 and CHOCHO, *Atmospheric Measurement Techniques*, 4, 2421-2439,
685 <https://doi.org/10.5194/amt-4-2421-2011>, 2011.

686 Crutzen, P. J.: The influence of nitrogen oxides on the atmospheric ozone content, *Quarterly*
687 *Journal of the Royal Meteorological Society*, 96, 320-325, <https://doi.org/10.1002/qj.49709640815>,
688 1970.

689 Cuevas, C. A., Maffezzoli, N., Corella, J. P., Spolaor, A., Vallelonga, P., Kjær, H. A., Simonsen, M.,
690 Winstrup, M., Vinther, B., Horvat, C., Fernandez, R. P., Kinnison, D., Lamarque, J. F., Barbante,
691 C., and Saiz-Lopez, A.: Rapid increase in atmospheric iodine levels in the North Atlantic since the
692 mid-20th century, *Nature Communications*, 9, 1452, <https://doi.org/10.1038/s41467-018-03756-1>,
693 2018.

694 Dameris, M., Loyola, D. G., Nützel, M., Coldewey-Egbers, M., Lerot, C., Romahn, F., and van
695 Roozendaal, M.: Record low ozone values over the Arctic in boreal spring 2020, *Atmospheric*
696 *Chemistry and Physics*, 21, 617-633, <https://doi.org/10.5194/acp-21-617-2021>, 2021.

697 De Laat, A., Van Geffen, J., Stammes, P., Van Der A, R., Eskes, H., and Veefkind, J. P.: The
698 Antarctic stratospheric nitrogen hole: Southern Hemisphere and Antarctic springtime total
699 nitrogen dioxide and total ozone variability as observed by Sentinel-5p TROPOMI, *Atmospheric*
700 *Chemistry and Physics*, 24, 4511-4535, <https://doi.org/10.5194/acp-24-4511-2024>, 2024.

701 Fleischmann, O. C., Hartmann, M., Burrows, J. P., and Orphal, J.: New ultraviolet absorption
702 cross-sections of BrO at atmospheric temperatures measured by time-windowing Fourier
703 transform spectroscopy, *Journal of Photochemistry and Photobiology A: Chemistry*, 168, 117-132,
704 <https://doi.org/10.1016/j.jphotochem.2004.03.026>, 2004.

705 Frieß, U., Wagner, T., Pundt, I., Pfeilsticker, K., and Platt, U.: Spectroscopic measurements of
706 tropospheric iodine oxide at Neumayer Station, Antarctica, *Geophysical Research Letters*, 28,
707 1941-1944, <https://doi.org/10.1029/2000GL012784>, 2001.

708 Frieß, U., Hollwedel, J., König-Langlo, G., Wagner, T., and Platt, U.: Dynamics and chemistry of
709 tropospheric bromine explosion events in the Antarctic coastal region, *Journal of Geophysical*
710 *Research (Atmospheres)*, 109, D06305, <https://doi.org/10.1029/2003JD004133>, 2004.

711 Frieß, U., Deutschmann, T., Gilfedder, B. S., Weller, R., and Platt, U.: Iodine monoxide in the
712 Antarctic snowpack, *Atmospheric Chemistry and Physics*, 10, 2439-2456,
713 <https://doi.org/10.5194/acp-10-2439-2010>, 2010.

714 Frieß, U., Sihler, H., Sander, R., Pöhler, D., Yilmaz, S., and Platt, U.: The vertical distribution of

715 BrO and aerosols in the Arctic: Measurements by active and passive differential optical absorption
716 spectroscopy, *Journal of Geophysical Research: Atmospheres*, 116,
717 <https://doi.org/10.1029/2011JD015938>, 2011.

718 Frieß, U., Klein Baltink, H., Beirle, S., Clémer, K., Hendrick, F., Henzing, B., Irie, H., de Leeuw,
719 G., Li, A., Moerman, M. M., van Roozendaal, M., Shaiganfar, R., Wagner, T., Wang, Y., Xie, P.,
720 Yilmaz, S., and Zieger, P.: Intercomparison of aerosol extinction profiles retrieved from
721 MAX-DOAS measurements, *Atmospheric Measurement Techniques*, 9, 3205-3222,
722 <https://doi.org/10.5194/amt-9-3205-2016>, 2016.

723 Frieß, U., Kreher, K., Querel, R., Schmithüsen, H., Smale, D., Weller, R., and Platt, U.: Source
724 mechanisms and transport patterns of tropospheric bromine monoxide: findings from long-term
725 multi-axis differential optical absorption spectroscopy measurements at two Antarctic stations,
726 *Atmospheric Chemistry and Physics*, 23, 3207-3232, <https://doi.org/10.5194/acp-23-3207-2023>,
727 2023.

728 Giesse, C., Notz, D., and Baehr, J.: On the Origin of Discrepancies Between Observed and
729 Simulated Memory of Arctic Sea Ice, *Geophysical Research Letters*, 48, e91784,
730 <https://doi.org/10.1029/2020GL091784>, 2021.

731 Gong, W., Beagley, S. R., Toyota, K., Skov, H., Christensen, J. H., Lupu, A., Pendlebury, D.,
732 Zhang, J., Im, U., Kanaya, Y., Saiz-Lopez, A., Sommariva, R., Effertz, P., Halfacre, J. W., Jepsen,
733 N., Kivi, R., Koenig, T. K., Müller, K., Nordstrøm, C., Petropavlovskikh, I., Shepson, P. B.,
734 Simpson, W. R., Solberg, S., Staebler, R. M., Tarasick, D. W., Van Malderen, R., and Vestenius, M.:
735 Modelling Arctic lower-tropospheric ozone: processes controlling seasonal variations,
736 *Atmospheric Chemistry and Physics*, 25, 8355-8405, <https://doi.org/10.5194/acp-25-8355-2025>,
737 2025.

738 Grebmeier, J. M., Overland, J. E., Moore, S. E., Farley, E. V., Carmack, E. C., Cooper, L. W., Frey,
739 K. E., Helle, J. H., McLaughlin, F. A., and McNutt, S. L.: A Major Ecosystem Shift in the
740 Northern Bering Sea, *Science*, 311, 1461-1464, 2006.

741 Hao, Y., Li, P., Gou, Y., Wang, Z., Tian, M., Chen, Y., Kuang, Y., Xu, H., Wan, F., Luo, Y., Huang,
742 W., and Chen, J.: Divergent changes in aerosol optical hygroscopicity and new particle formation
743 during a heatwave of summer 2022, *Atmospheric Chemistry and Physics*, 25, 12811-12830,
744 <https://doi.org/10.5194/acp-25-12811-2025>, 2025.

745 Hara, K., Osada, K., Yabuki, M., Matoba, S., Hirabayashi, M., Fujita, S., Nakazawa, F., and
746 Yamanouchi, T.: Atmospheric sea-salt and halogen cycles in the Antarctic, *Environmental Science:
747 Processes and Impacts*, 22, 2003-2022, <https://doi.org/10.1039/D0EM00092B>, 2020.

748 Hendrick, F., Van Roozendaal, M., Chipperfield, M. P., Dorf, M., Goutail, F., Yang, X., Fayt, C.,
749 Hermans, C., Pfeilsticker, K., Pommereau, J.-P., Pyle, J. A., Theys, N., and De Mazière, M.:
750 Retrieval of stratospheric and tropospheric BrO profiles and columns using ground-based
751 zenith-sky DOAS observations at Harestua, 60° N, *Atmospheric Chemistry and Physics*, 7,

752 4869-4885, <https://doi.org/10.5194/acp-7-4869-2007>, 2007.

753 Hindley, N. P., Wright, C. J., Smith, N. D., Hoffmann, L., Holt, L. A., Alexander, M. J.,
754 Moffat-Griffin, T., and Mitchell, N. J.: Gravity waves in the winter stratosphere over the Southern
755 Ocean: high-resolution satellite observations and 3-D spectral analysis, *Atmospheric Chemistry
756 and Physics*, 19, 15377-15414, <https://doi.org/10.5194/acp-19-15377-2019>, 2019.

757 Hong, Q., Liu, C., Chan, K. L., Hu, Q., Xie, Z., Liu, H., Si, F., and Liu, J.: Ship-based
758 MAX-DOAS measurements of tropospheric NO₂, SO₂, and HCHO distribution along the Yangtze
759 River, *Atmospheric Chemistry and Physics*, 18, 5931–5951,
760 <https://doi.org/10.5194/acp-18-5931-2018>, 2018.

761 Hwang, J. H. and Kang, D. W.: Emission Control Routes in Liner Shipping between Korea and
762 Japan, *Journal of Marine Science and Engineering*, 11, 2250,
763 <https://doi.org/10.3390/jmse11122250>, 2023.

764 Jozef, G. C., Cassano, J. J., Dahlke, S., Dice, M., Cox, C. J., and de Boer, G.: An overview of the
765 vertical structure of the atmospheric boundary layer in the central Arctic during MOSAiC,
766 *Atmospheric Chemistry and Physics*, 24, 1429–1450, <https://doi.org/10.5194/acp-24-1429-2024>,
767 2024.

768 Khosravi, S., Rinke, A., Dorn, W., Lüpkes, C., Gryanik, V., Chechin, D., Jaiser, R., and Handorf,
769 D.: The role of air-sea ice-ocean interaction processes for Arctic-midlatitude linkages,
770 <https://doi.org/10.5194/egusphere-egu2020-15116>, 2020.

771 Kuhlmann, G., Hartl, A., Cheung, H. M., Lam, Y. F., and Wenig, M. O.: A novel gridding
772 algorithm to create regional trace gas maps from satellite observations, *Atmospheric Measurement
773 Techniques*, 7, 451–467, <https://doi.org/10.5194/amt-7-451-2014>, 2014.

774 Luo, Y., Si, F., Zhou, H., Dou, K., Liu, Y., and Liu, W.: Observations and source investigations of
775 the boundary layer bromine monoxide (BrO) in the Ny-Ålesund Arctic, *Atmospheric Chemistry
776 and Physics*, 18, 9789–9801, <https://doi.org/10.5194/acp-18-9789-2018>, 2018.

777 Mahajan, A. S., Biswas, M. S., Beirle, S., Wagner, T., Schönhardt, A., Benavent, N., and
778 Saiz-Lopez, A.: Observations of iodine monoxide over three summers at the Indian Antarctic
779 bases of Bharati and Maitri, *Atmospheric Chemistry and Physics*, 21, 11829–11842,
780 <https://doi.org/10.5194/acp-21-11829-2021>, 2021.

781 Mahajan, A. S., Wagh, S., Fernandez, R. P., Singh, S., Bucci, S., and Saiz-Lopez, A.: Differences
782 in iodine chemistry over the Antarctic continent, *Polar Science*, 40, 101014,
783 <https://doi.org/10.1016/j.polar.2023.101014>, 2024.

784 McFiggans, G., Plane, J. M. C., Allan, B. J., Carpenter, L. J., Coe, H., and O'Dowd, C.: A
785 modeling study of iodine chemistry in the marine boundary layer, *Journal of Geophysical
786 Research Atmospheres*, 105, 14371–14385, <https://doi.org/10.1029/1999JD901187>, 2000.

787 McPhee, M. G.: The sea ice–ocean boundary layer, Book Title: Sea Ice. DOI:
788 10.1002/9781118778371.ch5, 138–159, <https://doi.org/10.1002/9781118778371.ch5>, 2017.

789 Meller, R. and Moortgat, G. K.: Temperature dependence of the absorption cross sections of
790 formaldehyde between 223 and 323 K in the wavelength range 225–375 nm, *Journal of*
791 *Geophysical Research Atmospheres*, 105, 7089–7101, <https://doi.org/10.1029/1999JD901074>,
792 2000.

793 Moore, C. W., Obrist, D., Steffen, A., Staebler, R. M., Douglas, T. A., Richter, A., and Nghiem, S.
794 V.: Convective forcing of mercury and ozone in the Arctic boundary layer induced by leads in sea
795 ice, *Nature*, 506, 81–84, <https://doi.org/10.1038/nature12924>, 2014.

796 Nasse, J.-M., Zielcke, J., Frieß, U., Lampel, J., König-Langlo, G., and Platt, U.: Inference of cloud
797 altitude and optical properties from MAX-DOAS measurements, *EGU General Assembly*
798 *Conference Abstracts*, ADS Bibcode: 2015 EGUGA.17.7232N, 7232, 2015a.

799 Nasse, J.-M., Zielcke, J., Lampel, J., Buxmann, J., Frieß, U., and Platt, U.: Vertical distribution of
800 tropospheric BrO in the marginal sea ice zone of the Northern Weddell Sea, *EGU General*
801 *Assembly Conference Abstracts*, ADS Bibcode: 2015 EGUGA.17.7150N, 7150, 2015b.

802 Park, J., Kang, H., Gim, Y., Jang, E., Park, K.-T., Park, S., Jung, C. H., Ceburnis, D., O’Dowd, C.,
803 and Yoon, Y. J.: New particle formation leads to enhanced cloud condensation nuclei
804 concentrations on the Antarctic Peninsula, *Atmospheric Chemistry and Physics*, 23, 13625–13646,
805 <https://doi.org/10.5194/acp-23-13625-2023>, 2023.

806 Pernov, J. B., Bossi, R., Lebourgeois, T., Nøjgaard, J. K., Holzinger, R., Hjorth, J. L., and Skov, H.:
807 Atmospheric VOC measurements at a High Arctic site: characteristics and source apportionment,
808 *Atmospheric Chemistry and Physics*, 21, 2895–2916, <https://doi.org/10.5194/acp-21-2895-2021>,
809 2021.

810 Peterson, P. K., Pöhler, D., Sihler, H., Zielcke, J., General, S., Frieß, U., Platt, U., Simpson, W. R.,
811 Nghiem, S. V., Shepson, P. B., Stirm, B. H., Dhaniyala, S., Wagner, T., Caulton, D. R., Fuentes, J.
812 D., and Pratt, K. A.: Observations of bromine monoxide transport in the Arctic sustained on
813 aerosol particles, *Atmospheric Chemistry and Physics*, 17, 7567–7579,
814 <https://doi.org/10.5194/acp-17-7567-2017>, 2017.

815 Polissar, A. V., Hopke, P. K., and Harris, J. M.: Source regions for atmospheric aerosol measured
816 at Barrow, Alaska, *Environmental Science and Technology*, 35, 4214–4226,
817 <https://doi.org/10.1021/es0107529>, 2001.

818 Polvani, L. M., Previdi, M., England, M. R., Chiodo, G., and Smith, K. L.: Substantial
819 twentieth-century Arctic warming caused by ozone-depleting substances, *Nature Climate Change*,
820 10, 130–133, <https://doi.org/10.1038/s41558-019-0677-4>, 2020.

821 Prados-Roman, C., Gómez-Martín, L., Puente-dura, O., Navarro-Comas, M., Iglesias, J., de Mingo,
822 J. R., Pérez, M., Ochoa, H., Barlasina, M. E., Carbajal, G., and Yela, M.: Reactive bromine in the
823 low troposphere of Antarctica: estimations at two research sites, *Atmospheric Chemistry and*
824 *Physics*, 18, 8549–8570, <https://doi.org/10.5194/acp-18-8549-2018>, 2018.

825 Pratt, K. A., Custard, K. D., Shepson, P. B., Douglas, T. A., Pöhler, D., General, S., Zielcke, J.,

826 Simpson, W. R., Platt, U., Tanner, D. J., Gregory Huey, L., Carlsen, M., and Stirm, B. H.:
827 Photochemical production of molecular bromine in Arctic surface snowpacks, *Nature Geosci*, 6,
828 351–356, <https://doi.org/10.1038/ngeo1779>, 2013.

829 Ranjithkumar, A., Duncan, E., Yang, X., Partridge, D., and Frey, M.: Modelling sea-salt aerosol
830 flux from blowing snow over a changing sea ice environment, EGU General Assembly
831 Conference Abstracts, EGU-6988, <https://doi.org/10.5194/egusphere-egu23-6988>, 2023.

832 Richter, A., Wittrock, F., Eisinger, M., and Burrows, J. P.: GOME observations of tropospheric
833 BrO in northern hemispheric spring and summer 1997, *Geophysical Research Letters*, 25,
834 2683–2686, <https://doi.org/10.1029/98GL52016>, 1998.

835 Roy, R., Kumar, P., Kuttippurath, J., and Lefevre, F.: Chemical ozone loss and chlorine activation
836 in the Antarctic winters of 2013–2020, *Atmospheric Chemistry and Physics*, 24, 2377–2386,
837 <https://doi.org/10.5194/acp-24-2377-2024>, 2024.

838 Rozanov, A., Rozanov, V., Buchwitz, M., Kokhanovsky, A., and Burrows, J. P.: SCIATRAN 2.0 –
839 A new radiative transfer model for geophysical applications in the 175–2400 nm spectral region,
840 *Advances in Space Research*, 36, 1015–1019, <https://doi.org/10.1016/j.asr.2005.03.012>, 2005.

841 Saiz-Lopez, A., Mahajan, A. S., Salmon, R. A., Bauguitte, S. J.-B., Jones, A. E., Roscoe, H. K.,
842 and Plane, J. M. C.: Boundary Layer Halogens in Coastal Antarctica, *Science*, 317, 348–351,
843 <https://doi.org/10.1126/science.1141408>, 2007.

844 Saiz-Lopez, A., Plane, J. M. C., Mahajan, A. S., Anderson, P. S., Bauguitte, S. J.-B., Jones, A. E.,
845 Roscoe, H. K., Salmon, R. A., Bloss, W. J., Lee, J. D., and Heard, D. E.: On the vertical
846 distribution of boundary layer halogens over coastal Antarctica: implications for O₃, HO_x, NO_x
847 and the Hg lifetime, *Atmospheric Chemistry and Physics*, 8, 887–900,
848 <https://doi.org/10.5194/acp-8-887-2008>, 2008.

849 Saiz-Lopez, A., Baidar, S., Cuevas, C. A., Koenig, T. K., Fernandez, R. P., Dix, B., Kinnison, D.
850 E., Lamarque, J.-F., Rodriguez-Lloveras, X., Campos, T. L., and Volkamer, R.: Injection of iodine
851 to the stratosphere, *Geophysical Research Letters*, 42, 6852–6859,
852 <https://doi.org/10.1002/2015GL064796>, 2015.

853 Seo, S., Richter, A., Blechschmidt, A.-M., Bougoudis, I., and Burrows, J. P.: Spatial distribution of
854 enhanced BrO and its relation to meteorological parameters in Arctic and Antarctic sea-ice regions,
855 *Atmospheric Chemistry and Physics*, 20, 12285–12312,
856 <https://doi.org/10.5194/acp-20-12285-2020>, 2020.

857 Serdyuchenko, A., Gorshelev, V., Weber, M., Chehade, W., and Burrows, J. P.: High spectral
858 resolution ozone absorption cross-sections and ndash; Part 2: Temperature dependence,
859 *Atmospheric Measurement Techniques*, 7, 625–636, <https://doi.org/10.5194/amt-7-625-2014>,
860 2014.

861 Shupe, M. D., Persson, P. O. G., Brooks, I. M., Tjernström, M., Sedlar, J., Mauritsen, T., Sjogren,
862 S., and Leck, C.: Cloud and boundary layer interactions over the Arctic sea-ice in late summer,

863 Atmospheric Chemistry and Physics, 13, 9379–9399, <https://doi.org/10.5194/acp-13-9379-2013>,
864 2013.

865 Simpson, W. R., Peterson, P. K., Frieß, U., Sihler, H., Lampel, J., Platt, U., Moore, C., Pratt, K.,
866 Shepson, P., Halfacre, J., and Nghiem, S. V.: Horizontal and vertical structure of reactive bromine
867 events probed by bromine monoxide MAX-DOAS, Atmospheric Chemistry and Physics, 17,
868 9291–9309, <https://doi.org/10.5194/acp-17-9291-2017>, 2017.

869 Song, Y., Xing, C., Liu, C., Lin, J., Wu, H., Liu, T., Lin, H., Zhang, C., Tan, W., Ji, X., Liu, H., and
870 Li, Q.: Evaluation of transport processes over North China Plain and Yangtze River Delta using
871 MAX-DOAS observations, Atmospheric Chemistry and Physics, 23, 1803–1824,
872 <https://doi.org/10.5194/acp-23-1803-2023>, 2023.

873 Spagnesi, A., Barbaro, E., Feltracco, M., Scoto, F., Vecchiato, M., Vardè, M., Mazzola, M., Burgay,
874 F. Y., Bruschi, F., Hoppe, C. J. M., Bailey, A., Gambaro, A., Barbante, C., and Spolaor, A.: Impact
875 of Arctic Amplification variability on the chemical composition of the snowpack in Svalbard,
876 EGU sphere, 1–25, <https://doi.org/10.5194/egusphere-2024-1393>, 2024.

877 Stutz, J. and Platt, U.: Numerical analysis and estimation of the statistical error of differential
878 optical absorption spectroscopy measurements with least-squares methods, Applied Optics, AO,
879 35, 6041–6053, <https://doi.org/10.1364/AO.35.006041>, 1996.

880 Stutz, J., Kim, E. S., Platt, U., Bruno, P., Perrino, C., and Febo, A.: UV-visible absorption cross
881 sections of nitrous acid, Journal of Geophysical Research, 105, 14,585–14,592,
882 <https://doi.org/10.1029/2000JD900003>, 2000.

883 Swanson, W. F., Graham, K. A., Halfacre, J. W., Holmes, C. D., Shepson, P. B., and Simpson, W.
884 R.: Arctic Reactive Bromine Events Occur in Two Distinct Sets of Environmental Conditions: A
885 Statistical Analysis of 6 Years of Observations, Journal of Geophysical Research: Atmospheres,
886 125, e2019JD032139, <https://doi.org/10.1029/2019JD032139>, 2020.

887 Tack, F., Hendrick, F., Goutail, F., Fayt, C., Merlaud, A., Pinardi, G., Hermans, C., Pommereau,
888 J.-P., and Van Roozendael, M.: Tropospheric nitrogen dioxide column retrieval from ground-based
889 zenith–sky DOAS observations, Atmospheric Measurement Techniques, 8, 2417–2435,
890 <https://doi.org/10.5194/amt-8-2417-2015>, 2015.

891 Tan, W., Liu, C., Wang, S., Xing, C., Su, W., Zhang, C., Xia, C., Liu, H., Cai, Z., and Liu, J.:
892 Tropospheric NO₂, SO₂, and HCHO over the East China Sea, using ship-based MAX-DOAS
893 observations and comparison with OMI and OMPS satellite data, Atmospheric Chemistry and
894 Physics, 18, 15387–15402, <https://doi.org/10.5194/acp-18-15387-2018>, 2018.

895 Thalman, R. and Volkamer, R.: Temperature dependent absorption cross-sections of O₂-O₂
896 collision pairs between 340 and 630 nm and at atmospherically relevant pressure, Physical
897 Chemistry Chemical Physics, 15, 15371–15381, <https://doi.org/10.1039/c3cp50968k>, 2013.

898 Theys, N., Van Roozendael, M., Hendrick, F., Yang, X., De Smedt, I., Richter, A., Begoin, M.,
899 Errera, Q., Johnston, P. V., Kreher, K., and De Mazière, M.: Global observations of tropospheric

900 BrO columns using GOME-2 satellite data, *Atmospheric Chemistry and Physics*, 11, 1791–1811,
901 <https://doi.org/10.5194/acp-11-1791-2011>, 2011.

902 Tremblay, S., Picard, J.-C., Bachelder, J. O., Lutsch, E., Strong, K., Fogal, P., Leitch, W. R.,
903 Sharma, S., Kolonjari, F., Cox, C. J., Chang, R. Y.-W., and Hayes, P. L.: Characterization of
904 aerosol growth events over Ellesmere Island during the summers of 2015 and 2016, *Atmospheric*
905 *Chemistry and Physics*, 19, 5589–5604, <https://doi.org/10.5194/acp-19-5589-2019>, 2019.

906 Vandaele, A. C., Hermans, C., Simon, P. C., Carleer, M., Colin, R., Fally, S., Mérienne, M. F.,
907 Jenouvrier, A., and Coquart, B.: Measurements of the NO₂ absorption cross-section from 42000
908 cm⁻¹ to 10 000 cm⁻¹ (238–1000 nm) at 220 K and 294 K, *Journal of Quantitative Spectroscopy*
909 *and Radiative Transfer*, 59, 171–184, [https://doi.org/10.1016/S0022-4073\(97\)00168-4](https://doi.org/10.1016/S0022-4073(97)00168-4), 1998.

910 Wagner, T., Ibrahim, O., Sinreich, R., Frieß, U., von Glasow, R., and Platt, U.: Enhanced
911 tropospheric BrO over Antarctic sea-ice in mid-winter observed by MAX-DOAS on board the
912 research vessel Polarstern, *Atmospheric Chemistry and Physics*, 7, 3129–3142,
913 <https://doi.org/10.5194/acp-7-3129-2007>, 2007.

914 Wagner, T., Ibrahim, O., Shaiganfar, R., and Platt, U.: Mobile MAX-DOAS observations of
915 tropospheric trace gases, *Atmospheric Measurement Techniques*, 3, 129–140,
916 <https://doi.org/10.5194/amt-3-129-2010>, 2010.

917 Wang, X., Shen, Y., Lin, Y., Pan, J., Zhang, Y., Louie, P. K. K., Li, M., and Fu, Q.: Ambient
918 measurement of shipping emissions in Shanghai port areas, <https://doi.org/10.5194/acp-2018-737>,
919 21 August 2018.

920 Welsh, B. A., Corrigan, M. E., Assaf, E., Nauta, K., Sebastianelli, P., Jordan, M. J. T., Fittschen, C.,
921 and Kable, S. H.: Photophysical oxidation of HCHO produces HO₂ radicals, *Nature Chemistry*, 15,
922 1350–1357, <https://doi.org/10.1038/s41557-023-01272-4>, 2023.

923 Wittrock, F., Oetjen, H., Richter, A., Fietkau, S., Medeke, T., Rozanov, A., and Burrows, J. P.:
924 MAX-DOAS measurements of atmospheric trace gases in Ny-Ålesund - Radiative transfer studies
925 and their application, *Atmospheric Chemistry and Physics*, 4, 955–966,
926 <https://doi.org/10.5194/acp-4-955-2004>, 2004.

927 Wu, F., Xie, P., Li, A., Mou, F., Chen, H., Zhu, Y., Zhu, T., Liu, J., and Liu, W.: Investigations of
928 temporal and spatial distribution of precursors SO₂ and NO₂ vertical columns in the North China
929 Plain using mobile DOAS, *Atmospheric Chemistry and Physics*, 18, 1535–1554,
930 <https://doi.org/10.5194/acp-18-1535-2018>, 2018.

931 Yang, X., Blechschmidt, A.-M., Bognar, K., McClure-Begley, A., Morris, S., Petropavlovskikh, I.,
932 Richter, A., Skov, H., Strong, K., Tarasick, D. W., Uttal, T., Vestenius, M., and Zhao, X.:
933 Pan-Arctic surface ozone: modelling vs. measurements, *Atmospheric Chemistry and Physics*, 20,
934 15937–15967, <https://doi.org/10.5194/acp-20-15937-2020>, 2020.

935 Yang, Y., Zhao, C., Wang, Q., Cong, Z., Yang, X., and Fan, H.: Aerosol characteristics at the three
936 poles of the Earth as characterized by Cloud–Aerosol Lidar and Infrared Pathfinder Satellite

937 Observations, *Atmospheric Chemistry and Physics*, 21, 4849–4868,
938 <https://doi.org/10.5194/acp-21-4849-2021>, 2021.

939 Yin, X., Kang, S., de Foy, B., Ma, Y., Tong, Y., Zhang, W., Wang, X., Zhang, G., and Zhang, Q.:
940 Multi-year monitoring of atmospheric total gaseous mercury at a remote high-altitude site (Nam
941 Co, 4730m a.s.l.) in the inland Tibetan Plateau region, *Atmospheric Chemistry and Physics*, 18,
942 10557–10574, <https://doi.org/10.5194/acp-18-10557-2018>, 2018.

943 Zhao, X., Strong, K., Adams, C., Schofield, R., Yang, X., Richter, A., Friess, U., Blechschmidt,
944 A.-M., and Koo, J.-H.: A case study of a transported bromine explosion event in the Canadian high
945 arctic, *Journal of Geophysical Research: Atmospheres*, 121, 457–477,
946 <https://doi.org/10.1002/2015JD023711>, 2016.

947